UCLA
UCLA Electronic Theses and Dissertations

**Title**
Development of Mid-infrared and Far-infrared QCLs

**Permalink**
https://escholarship.org/uc/item/1r11x59r

**Author**
Shahili, Mohammad

**Publication Date**
2021

Peer reviewed|Thesis/dissertation

eScholarship.org Powered by the California Digital Library
University of California

UNIVERSITY OF CALIFORNIA

Los Angeles

# Development of Mid-infrared and Far-infrared QCLs

A thesis submitted in partial satisfaction
of the requirements for the degree
Master of Science in Electrical and Computer Engineering

by

Mohammad Shahili

2021

© Copyright by

Mohammad Shahili

2021

ABSTRACT OF THE THESIS

Development of Mid-infrared and Far-infrared QCLs

by

Mohammad Shahili
Master of Science in Electrical and Computer Engineering
University of California, Los Angeles, 2021
Professor Benjamin Williams, Chair

Mid-infrared Quantum Cascade Lasers (mid-IR QCLs) have been rapidly developing and becoming the practical mid-IR source for a multitude of applications. They are of particular technological interest as high efficiency lasers designed for the mid-wavelength infrared (MWIR) (3-5 $\mu$m), long-wavelength infrared (LWIR) (8-13 $\mu$m), and very-long-wavelength (VLWIR) (16-25 $\mu$m) atmospheric windows. Even though reasonably high efficiency has been achieved in mid-IR QCLs, a study of their efficiency based on an accurate transport modelling such as Non-equilibrium Green's Function (NEGF) is missing, probably due to its complicated and computationally intensive nature. In this work I focused on two sub-projects; first is the development of high efficiency QCLs at 5 $\mu$m, and second is the design of a QCL that operates at 20 $\mu$m. For both projects, I present the design, bandstructure modeling and simulation, detailed micro-fabrication process, and characterization results and methods.

The thesis of Mohammad Shahili is approved.

Robert Candler

Chandrashekhar Joshi

Benjamin Williams, Committee Chair

University of California, Los Angeles

2021

TABLE OF CONTENTS


**1 Introduction** . . . . . . . . . . . . . . . . . . . . . . . . . . . . . . **1**

1.1 Mid-IR region . . . . . . . . . . . . . . . . . . . . . . . . . . . . . 2

1.1.1 Applications . . . . . . . . . . . . . . . . . . . . . . . . . . . 2

1.1.2 Sources . . . . . . . . . . . . . . . . . . . . . . . . . . . . . 5

1.2 Quantum cascade lasers . . . . . . . . . . . . . . . . . . . . . . . . 6

1.3 Active regions survey . . . . . . . . . . . . . . . . . . . . . . . . . 8

1.4 Thesis overview . . . . . . . . . . . . . . . . . . . . . . . . . . . . 12

**2 Theory and Modeling** . . . . . . . . . . . . . . . . . . . . . . . . . **13**

2.1 Introduction . . . . . . . . . . . . . . . . . . . . . . . . . . . . . . 13

2.2 Electronic states . . . . . . . . . . . . . . . . . . . . . . . . . . . . 13

2.3 Intersubband transition and gain . . . . . . . . . . . . . . . . . . . 15

2.4 Scattering mechanisms and level lifetime . . . . . . . . . . . . . . . 18

2.4.1 LO phonon scattering . . . . . . . . . . . . . . . . . . . . . . 19

2.4.2 Interface roughness scattering . . . . . . . . . . . . . . . . . . 22

2.4.3 Alloy disorder scattering . . . . . . . . . . . . . . . . . . . . . 23

2.5 Schrödinger solver . . . . . . . . . . . . . . . . . . . . . . . . . . . 24

2.5.1 Shooting method . . . . . . . . . . . . . . . . . . . . . . . . . 24

2.5.2 Nonparabolicity . . . . . . . . . . . . . . . . . . . . . . . . . 27

2.5.3 Single quantum well solution . . . . . . . . . . . . . . . . . . . 28

**3 MWIR QCL: design, fabrication, characterization** . . . . . . . . . . . **30**

3.1 Introduction . . . . . . . . . . 30
3.1.1 Wall plug efficiency . . . . . . . . . . 31
3.1.2 Non-equilibrium Green's Function . . . . . . . . . . 33
3.2 Two-material design . . . . . . . . . . 34
3.3 Multi-material design . . . . . . . . . . 36
3.3.1 Rate equations versus NEGF calculation . . . . . . . . . . 38
3.3.2 Compare to original design . . . . . . . . . . 39
3.4 Fabrication development . . . . . . . . . . 41
3.4.1 Process flow . . . . . . . . . . 41
3.4.2 Challenges and solutions . . . . . . . . . . 43
3.5 Characterization . . . . . . . . . . 46
3.5.1 Equipment and setup . . . . . . . . . . 47
3.5.2 Forward Photonics device . . . . . . . . . . 48
3.5.3 Forward Photonics device - thin cladding . . . . . . . . . . 50

**4 VLWIR QCL: design, fabrication, characterization . . . . . . . . . . 52**
4.1 Introduction . . . . . . . . . . 52
4.2 Active region design . . . . . . . . . . 53
4.3 Waveguide design . . . . . . . . . . 56
4.4 Fabrication . . . . . . . . . . 57
4.5 Device characterization . . . . . . . . . . 60

**5 Conclusion . . . . . . . . . . 63**

**A Fabrication Process Flow . . . . . . . . . . 65**

A.1 Etch mask preparation . . . . . . . . . . 65
A.2 Ridge definition . . . . . . . . . . 66
A.3 Top window opening for electrical contact . . . . . . . . . . 67
A.4 Top contact deposition . . . . . . . . . . 68
A.5 Substrate lapping and bottom contact deposition . . . . . . . . . . 69

**B CV Characterization . . . . . . . . . . 71**

**References . . . . . . . . . . 73**

LIST OF FIGURES

1.1 The monolithic integration of a laser, a SPP waveguide and a detector for a lab-on-chip mid-infrared spectrometer, from Ref. [40]. . . . . . . . . . . . . . . . . 3

1.2 atmospheric transmission window, from Ref. [33] . . . . . . . . . . . . . . . . . . 4

1.3 Comparison of gain in an intersubband (a) and interband (b) systems at zero temperature, from Ref. [12]. . . . . . . . . . . . . . . . . . . . . . . . . . . . 6

1.4 Conduction band diagram of a portion of 25-period section of the first demonstrated QCL, from Ref. [14]. . . . . . . . . . . . . . . . . . . . . . . . . . . . 7

1.5 Conduction band diagram of (a) two-phonon resonance designed for operation at $\lambda \approx$9 $\mu$m and (b) bound-to-continuum active region designed for operation at $\lambda \approx$9.1 $\mu$m, from Ref. [12]. . . . . . . . . . . . . . . . . . . . . . . . . . . . 8

1.6 Conduction band diagram of (a) the Shallow well design for operation at $\lambda \approx$4.9 $\mu$m, from Ref. [2] and (b) two-material active region designed for operation at $\lambda \approx$5.6 $\mu$m, from Ref. [34]. . . . . . . . . . . . . . . . . . . . . . . . . . . . 10

2.1 Different classes of scattering processes: (a) elastic scattering; (b) inelastic scattering; (c) carrier-carrier scattering; from Ref. [23]. . . . . . . . . . . . . . . . . . 19

2.2 (a) Schematic illustration of intersubband LO-phonon scattering process. (b) Inplane reciprocal lattice space diagram illustrating the relationship between initial and final electron wavevectors $k_i$ and $k_f$ and in-plane phonon wavevector $q_{||}$, from Ref. [55]. . . . . . . . . . . . . . . . . . . . . . . . . . . . . . . . . . . 20

2.3 Numerically obtained wavefunctions above and below the true solution at E = 29.43 meV, for an electron in a 150°A $Ga_{0.8}Al_{0.2}As$/100°A GaAs/150°A $Ga_{0.8}Al_{0.2}As$ single quantum well, from Ref. [20]. . . . . . . . . . . . . . . . . . . . . . . . . . 25

2.4 Simulated bandstructure for GaAs/$Al_{0.15}$GaAs single finite quantum well using shooting method. . . . . . . . . . . . . . . . . . . . . . . . . . . . . . . . . 28

3.1 (a) Simulated bandstructure (electrostatic mean-field interactions are ignored) profile of FP 2-Material active region using shooting method Schrödinger solver. Well/barrier layers are strain-balanced $Al_{0.78}In_{0.22}As/In_{0.69}Ga_{0.31}As$, with average doping of $2.6\times10^{16}$ cm$^{-3}$ (b) Calculated anticrossing, energy separation, and oscillator strength versus electric field. The dotted line shows the design bias. . 35

3.2 (a) Simulated bandstructure (electrostatic mean-field interactions are ignored) profile of the revised shallow-well design using shooting method Schrödinger solver and (b) the simulated bandstructure of the original shallow-well design [2]. . . . 37

3.3 (a) Simulated gain using NEGF for the original shallow-well design compared to the revised design (b) Comparison of the simulated gain using rate equations and NEGF for the revised shallow-well design. . . . . . . . . . . . . . . . . . . . . . 38

3.4 Simulated (a) current-voltage characteristics of the original and revised shallow well design and (b) WPE and power density calculated using NEGF solver in nextnano package. Photon-assisted transport is enabled for an EM mode at 270 meV. . . . . . . . . . . . . . . . . . . . . . . . . . . . . . . . . . . . . . . 40

3.5 MWIR QCL ridge fabrication process flow. . . . . . . . . . . . . . . . . . . . . . 42

3.6 HCl:$CH_3COOH$ etch profile for ridge oriented (a) perpendicular and (b) parallel to the wafer major flat. HBr:$HNO_3$:$H_2O$ etch profile for ridge oriented (c) perpendicular and (d) parallel to the wafer major flat. Result provided by Dr. Sudeep Khanal. . . . . . . . . . . . . . . . . . . . . . . . . . . . . . . . . . . . 44

3.7 Photoresist delamination after HBr wet etch. . . . . . . . . . . . . . . . . . . . . 45

3.8 Top contact evaporated (a) vertically and (b) at an angle. . . . . . . . . . . . 46

3.9 Characterization setup for (a) light-current-voltage measurement and (b) electro-luminescence measurement. . . . . . . . . . . . . . . . . . . . . . . . . . . . 47

3.10 (a) 223F3-BNL48-00 temperature dependent L-I-V and (b) wall plug efficiency. (c) Spectra at room temperature and 1% duty cycle. . . . . . . . . . . . . . . 49

3.11 (a) 22851-BNL48-01 temperature dependent L-I-V for the 8 $\mu$m ridge. (b) Cross section SEM of the fabricated 25 $\mu$m ridge. (c) Spectra at 77 K and (d) electro-luminescence at 300 K. . . . . . . . . . . . . . . . . . . . . . . . . . . . . 51

4.1 Bandstructure of the 20 $\mu$m QCL. . . . . . . . . . . . . . . . . . . . . . . . . 53

4.2 LO phonon scattering times versus bias for lattice temperature of 300 K. . . . . 54

4.3 NEGF simulation of gain versus lattice temperature for 20 $\mu$m QCL. . . . . . . 55

4.4 (a) Surface plasmon and (b) MM waveguide mode profile. . . . . . . . . . . . . 56

4.5 Fabrication process flow for 20 $\mu$m QCL. . . . . . . . . . . . . . . . . . . . . 58

4.6 (a) Piece after InP etch using HCl:$H_3PO_4$ (1:3) solution and (b) dry etch profile using ULVAC NE-550 Chlorine etcher. . . . . . . . . . . . . . . . . . . . . . 60

4.7 (a) Current-voltage characteristics of 200 um diameter mesa versus temperature and (b) light-current-voltage characteristics of 50 $\mu$m wide 1 mm length MM waveguide ridge at 78 K. . . . . . . . . . . . . . . . . . . . . . . . . . . . . 61

4.8 (a) Bias dependent spectra of the 50 $\mu$m wide 1 mm long MM waveguide ridge laser and (b) its temperature dependent spectra. . . . . . . . . . . . . . . . . . . 62

B.1 (a) Capacitance-voltage characterization setup and (b) C-V measurement of device VA1033 . . . . . . . . . . . . . . . . . . . . . . . . . . . . . . . . . . 72

LIST OF TABLES

2.1 Theoretical versus simulated values for the eigenenergies of single finite quantum well. . . . . . . . . . . . . . . . . . . . . . . . . . . . . . . . . . . . . . . . . . . 29

## ACKNOWLEDGMENTS

First and foremost, I would like to thank my advisor Professor Benjamin Williams, for giving me the opportunity for being part of so many interesting projects, and teaching and mentoring me along the way like no other. Professor Williams was a huge source of encouragement during the hardships and downs of the research, and never shied away from helping me by being a great mentor and source of knowledge.

I would also like to thank the members of the committee, Professor Robert Candler, and Professor Chan Joshi, for the time they put in for me and all the valuable comments and discussions. As my undergraduate advisor, Professor Candler has always been there for me to answer my questions and being a great source of knowledge throughout my undergraduate career, as well as giving me the opportunity to work in their lab as an undergraduate researcher.

This work was partially supported by funding from National Science Foundation and Forward Photonics.

Special thanks goes to my current and former labmates: Eilam Morag, Yu Wu, Anthony Kim, Yue Shen, Jordane Bloomfield, Parastou Mortazavian (now at Apple) and Dr. Christopher Curwen (now at JPL). I am grateful to Dr. Curwen for all the illuminating discussions we had, and for always being there to answer my questions.

Finally, my biggest thank you goes to my family for always supporting me throughout not only my graduate career, but also in every other aspect of my life. I could not have made it this far without their endless love and support.

# CHAPTER 1

# Introduction

Laser diodes with operating wavelengths from near-infrared (near-IR) to the visible have been used in a variety of applications such as laser printers, supermarket scanners, and laser pointers, to name a few. Their operation principle is usually straightforward: the laser active region, which is a semiconductor material with a specific bandgap, is injected with electrons and holes which will recombine and emit a photon of energy equal to the bandgap. The spontaneously emitted photon is multiplied in a cavity through stimulated emission, and a coherent beam of photons is created which we know as the laser beam. To change the wavelength of the laser, one needs to use a material with a different bandgap, which can completely differ in electronic and optical properties.

There are some well-known limitations associated with these interband lasers. First, the dependence of the laser frequency on the bandgap limits the performance of the device as well as putting a limitation on the availability of a material with such a bandgap. This is especially true for the mid-infrared (mid-IR) range from 3 to 25 $\mu$m, known as the molecular fingerprint region, which is important for spectroscopy and gas sensing applications. As the bandgap of the material gets smaller, the effects of thermal runaway and thermal cycling degrade the laser performance. Second, the smaller bandgap of the material makes it more vulnerable to defects in the bandgap, also known as traps and recombination centers. This makes the device less reliable and decreases the yield. Additionally, as the bandgap of a material remains unchanged with the applied bias, tuning of the laser frequency is limited. For example, Lead-salt lasers give small power levels with limited tuning, and also have yet

to operate at room temperature.

Quantum cascade lasers (QCLs) have been able to surpass these limitations by providing high-power, single mode, and tunable sources in mid-IR and terahertz (THz), with the flexibility of changing the operation frequency while using the same material system. Their unique features and design flexibilities have made them a highly used source in commercial applications, as well as making them an extremely active field in the research and development community. In this chapter, I review some of the main applications of the mid-IR region, and provide a summary of the current state-of-the-art mid-IR QCL active regions.

## 1.1 Mid-IR region

### 1.1.1 Applications

The mid-IR region of the electromagnetic (EM) spectrum has always been an important area of research with many interesting applications. One important application is spectroscopy that can provide chemical, structural, and compositional information on the molecules, which have wide range of applications from material science [16], medicine [22] and biotechnology [10, 28], to environmental analysis [36, 24]. The detection of different trace gases and molecules comes from probing the rotational and vibrational transitions of the atoms in a molecule that provides a distinct spectral pattern, also known as the fingerprint of that molecule. This shows up in the spectral data as absorption lines, which can be used to find the analyte concentration and the molar absorption coefficient using the Beer-Lambert law. An emerging and active field of research in mid-IR spectroscopy tries to combine different components of a spectrometer such as the emitter, detector, external optics, and Fourier-transform infrared spectrometer (FTIR) into a monolithically integrated lab-on-a-chip for a compact and cost-effective sensing solution. An example was shown by the Strasser group, which combined a QCL and detector with a surface plasmon-polarition waveguide to detect water in ethanol via the absorption feature at 810 $cm^{-1}$ with a dynamic range of 0–60% at

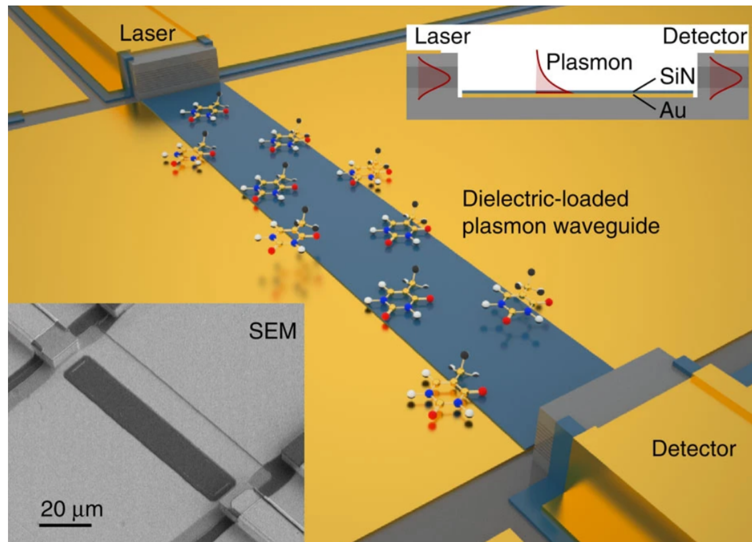


Figure 1.1: The monolithic integration of a laser, a SPP waveguide and a detector for a lab-on-chip mid-infrared spectrometer, from Ref. [40].

parts-per-million detection levels [40], as shown in Fig. 1.1. A viable source for spectroscopy needs to have high power, single frequency with broad tunability, as well as being compact, efficient, and operate at room temperature.

Another interesting application is in laser material processing. As opposed to laser cutting techniques that require very high power laser beams and is used to cut through different materials, mid-IR lasers can be used to selectively remove materials by exploiting the strong infrared absorption of some materials such as polymers. One example of this is controlled stripping of coatings from optical fibers for additional processing, termination, or packaging purposes.

The atmospheric transmission window in the mid-IR, shown in Fig. 1.2, is an attractive region for applications such as infrared countermeasures and free space communication, due to the lower absorption and signal distortion compared to the near-IR that is currently used [44]. Additionally, they provide high bandwidth with relatively high security to eavesdropping, while avoiding the complexity of installing optical fibers. Given that the atmospheric optical channel faces drastically different characteristics than the fiber-based channels, the

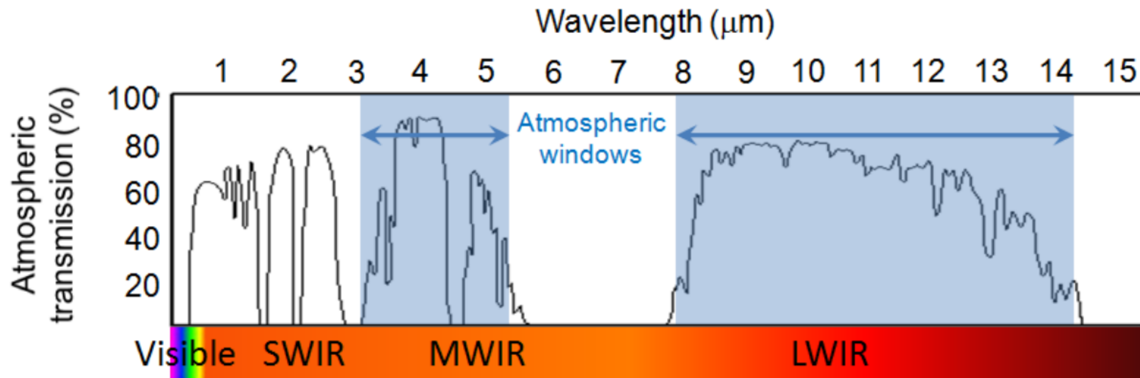


Figure 1.2: atmospheric transmission window, from Ref. [33]

choice of wavelength becomes increasingly important [35], and it is natural to search for sources with longer wavelengths than the ones used for the telecommunication systems. However, those sources need to be comparable in performance, if not better, than the existing telecommunication sources at 1.55 $\mu$m. The atmospheric windows at 3-5 $\mu$m and 8-10 $\mu$m can operate with lower solar glare, offer eye-safe operation, provide higher alignment tolerance, and experience less scattering with fog particles than near-IR. This comes with the cost of higher diffraction losses and larger size of the optics. The high frequency modulation capability and high operation power of QCLs are two factors that make them suitable for free space communications.

Last but not least, the thermal emission signature of objects with temperatures above 200 K, such as humans and animals, have spectral peaks in the mid-IR region. Therefore, this region of EM spectrum is of great importance for security and defense applications, such as thermal targeting and night vision [25]. The aforementioned applications, and many more that are not listed here, have spurred notable interest in developing high performing mid-IR sources, detectors, and optical elements. In the next section, I will touch on some of the important examples of sources used in this region.

### 1.1.2 Sources

One of the earliest and most widely used mid-IR sources are thermal emitters. They are basically heated objects, such as the 'glo-bar' in FTIR, that emit blackbody radiation at their body temperature. They are therefore broadband sources suitable for spectroscopy applications and are cost-effective. The downside to these types of emitters is their inefficiency and lack of coherence and tunability for applications that require emission in a narrow wavelength range.

Coherent sources such as $CO_2$ and CO lasers have been around and are still used in many applications. Their are however bulky and expensive to maintain, and are limited to a fixed set of emission lines [19]. Another way of achieving coherent sources in this region has been non-linear downconversion from near-IR fiber lasers. However, they are relatively complex systems and costly. The most straightforward and cost-effective source of coherent emission in this range of wavelength is arguably the interband quantum well diode lasers, such as the AlGaIn/AsSb diode laser [12]. However, they cannot operate at room temperature in the MWIR, and suffer from small bandgap effects such as Auger recombination.

The most successful, if not the least complex, sources of coherent mid-IR has been the interband cascade laser (ICL) and QCL. They both make use of the cascading scheme, with the main difference of radiative transition occurring between conduction and valence bands for ICL, and between intersubband states of the same band (conduction or valence) for QCL. Though ICLs are promising as coherent sources in the 3-7 $\mu$m range with low threshold current densities and transverse electric (TE) polarized emission, their operating temperature is limited compared to QCLs, and they generally exhibit lower slope efficiencies and peak powers.

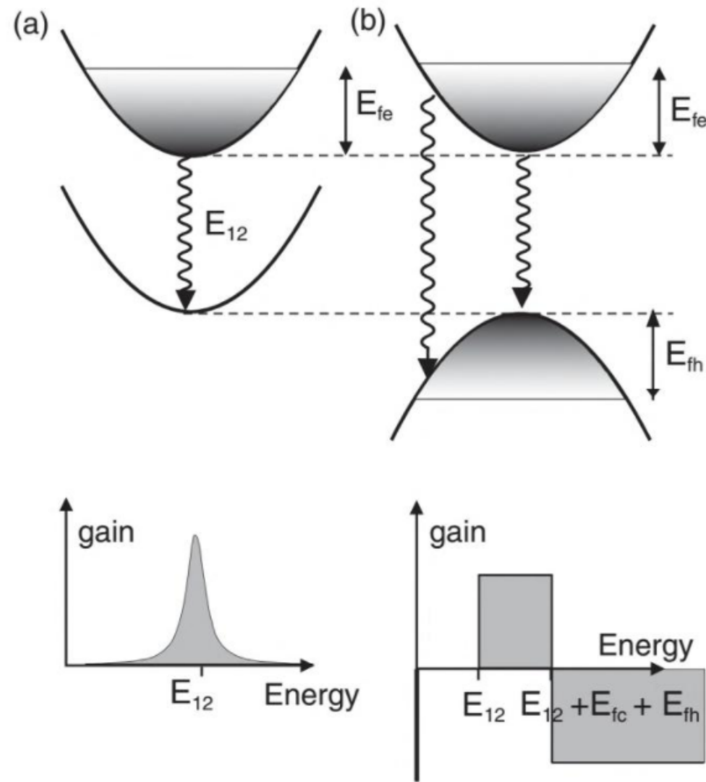


Figure 1.3: Comparison of gain in an intersubband (a) and interband (b) systems at zero temperature, from Ref. [12].

## 1.2 Quantum cascade lasers

The quantum cascade laser is a unipolar device which enables lasing at wavelengths spanning the mid-IR and part of the far-IR (3-28 $\mu$m) to THz (53-250 $\mu$m) regime, by exploiting optical transitions between electronic subbands which are created by spatial confinement in quantum wells. This makes the joint density of states delta-like similar to atomic systems, as opposed to a step-like gain for interband lasers, as shown in Fig. 1.3. The enabling feature of QCLs lies in the bandgap engineering, by stacking layers of lattice-matched or strain-balanced materials with different bandgaps, and adjusting the width of the layers to achieve specific energy differences between the lasing levels. Of course, this would not have

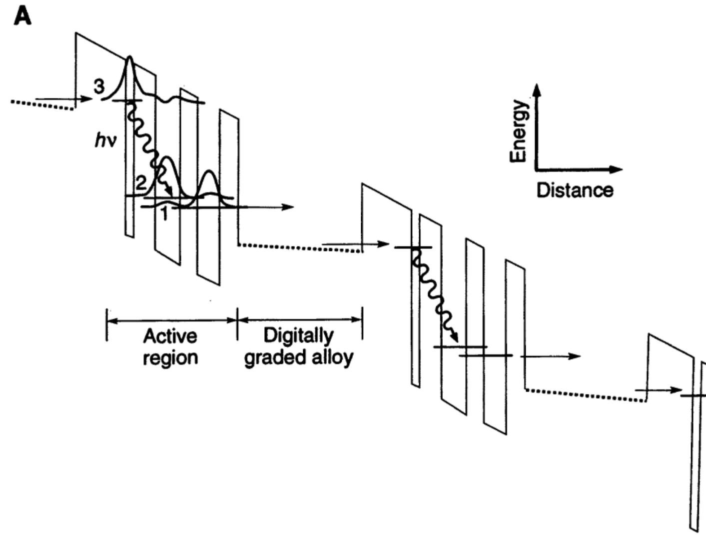


Figure 1.4: Conduction band diagram of a portion of 25-period section of the first demonstrated QCL, from Ref. [14].

been possible if it were not for the immense advancement in the field of epitaxial growth of semiconductors through molecular beam epitaxy (MBE) and metal-organic chemical vapour deposition (MOCVD).

The idea of intersubband transition goes back to the work of Kazarinov and Suris in 1971 on superlattice structures [29], and was first demonstrated successfully in Bell Labs in 1994 [14]. Since then, QCLs have evolved rapidly and have become the main source of mid-IR lasers used in a myriad of applications. The first successful demonstration of QCL by Faist and coworkers in 1994 [14] was a 3 quantum well (3QW) active region based on $In_{0.53}Ga_{0.47}As/In_{0.52}Al_{0.48}As$, as shown in Fig. 1.4. This design achieved reasonable upper to lower state lifetime by combining optical phonon resonance with diagonal optical transition. The former ensures efficient carrier extraction from the lower level by the fast LO phonon scattering mechanism, while the latter increases the upper state lifetime by decreasing the oscillator strength of the transition. While this was an excellent achievement since the 25 year-long quest to realize such a device, it suffered from low temperature operation and

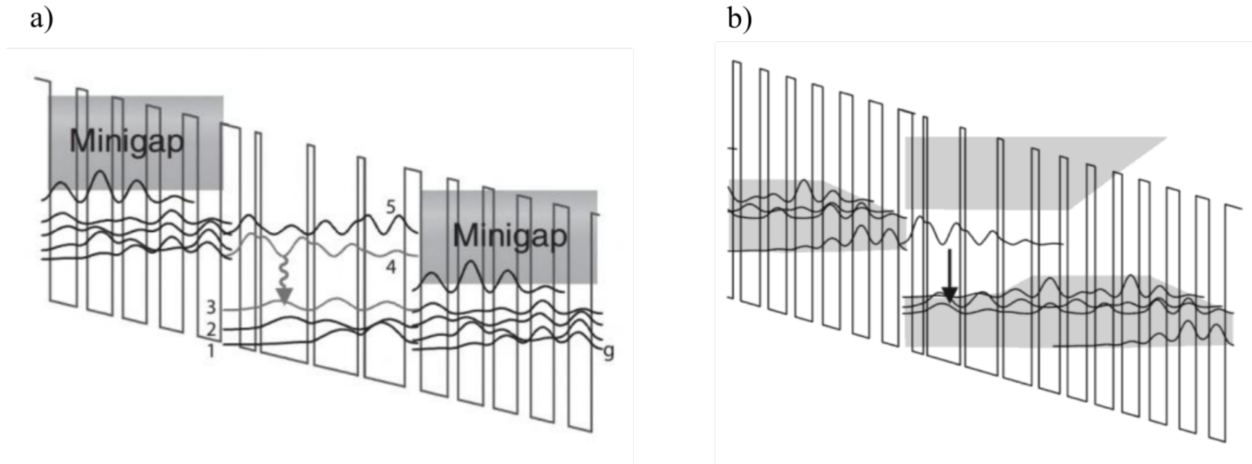


Figure 1.5: Conduction band diagram of (a) two-phonon resonance designed for operation at $\lambda \approx 9$ $\mu$m and (b) bound-to-continuum active region designed for operation at $\lambda \approx 9.1$ $\mu$m, from Ref. [12].

power levels and high threshold current density. It is worth mentioning that developing intersubband lasers in the THz was originally thought to be easier, where the non-radiative LO phonon emission would be energetically forbidden. However, this was proved to not be the case, and population inversion turned out to be easier to achieve in mid-IR QCLs where the subband separation is much higher than the LO phonon energy, and free carrier absorption is lower.

## 1.3 Active regions survey

Over the years, the mid-IR QCL active regions have gone through multiple changes to improve the device parameters such as operating temperature, output power levels, and wall plug efficiency (WPE). Due to the ease and higher quality of growth, the first generation of devices made use of the lattice matched $In_{0.53}Ga_{0.47}As/In_{0.52}Al_{0.48}As$ structure grown on InP. One important example is the double phonon resonance design, shown in Fig. 1.5a [4]. This design improved on the extraction of the ground level of the active region by placing

two levels below the lower laser level, all separated by an LO phonon energy. The addition of the third level improves the lower level extraction significantly compared to the 3QW design. This is because in the 3QW design, the extracted carriers are prone to be scattered back into the lower level due to the higher timescale of the resonant tunneling lifetime compared to the lower level scattering lifetime.

Another method for obtaining high population inversion was through the bound-to-continuum (BTC) design, shown in Fig. 1.5b [13]. This design takes advantage of two attractive features associated with superlattice active regions, namely the large oscillator strengths and the fast depopulation of the lower laser level at the edge of the minigap, as well as utilizing the large injection efficiency associated with the 3QW design. This BTC design has shown great promise in (1) achieving high temperature performance due to the low temperature dependence of the threshold current density, (2) long-wave operation due to the desirable lifetime ratios, (3) broadband gain due to having multiple lower levels, and (4) non-linear generation due to the active region exhibiting THz susceptibility, which enables THz generation by non-linear mixing up to room temperature [12].

In the optoelectronics community, the growth of strain-free and high crystalline quality has always been a prerequisite for achieving high performing semiconductor lasers. Thus growing lattice matched structures ensured growths of defect free structures without dislocations, and the QCL community also followed suit. However, it was eventually realized that growth of lattice mismatch layers can be of great importance since it provides another degree of freedom in the design, and this was achieved using strain-balancing. Since both signs of strain are present in a QCL structure, with the $In_xGa_{1-x}As$ wells being compressively strained and the $In_xAl_{1-x}As$ barriers being tensile strained, the layer widths and compositions can be selected such that the total strain on the InP substrate is zero, and the structure can be grown without defects [20]. This was perhaps the enabling feature in achieving high WPE mid-IR QCLs, since the great flexibility in conduction band offset facilitated the control over minimizing leakage channels and engineering the electronic band structures to achieve

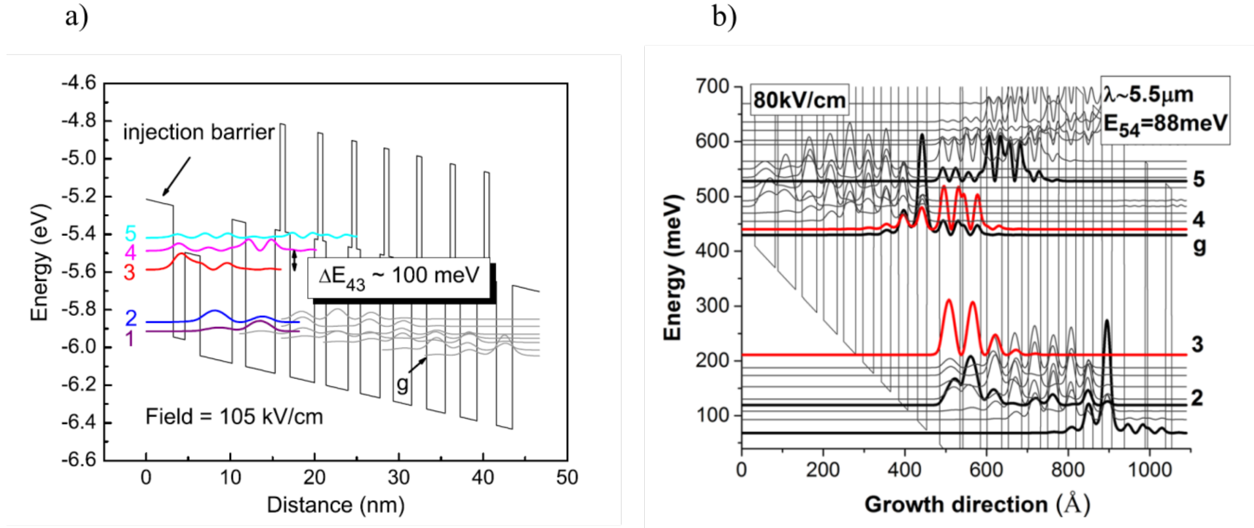


Figure 1.6: Conduction band diagram of (a) the Shallow well design for operation at $\lambda \approx$4.9 $\mu$m, from Ref. [2] and (b) two-material active region designed for operation at $\lambda \approx$5.6 $\mu$m, from Ref. [34].

high population inversion. So far, mid-IR QCLs with the highest WPE values make use of this idea as well as employing bandstructure engineering and waveguide design to minimize losses. Currently, pulsed WPE as high as 31% [53] and continuous wave WPE as high as 22% [54] at 4.9 $\mu$m has been achieved in the MWIR, and WPE up to 20.4% and 9.5% [59] has been achieved at 8 $\mu$m, for pulsed and continuous wave operation respectively, in the LWIR region.

As shown by Faist in [11], ignoring photon-driven transport, the theoretical maximum WPE takes the simplified form

$$\eta_{wp,max} = \eta_{tr} \frac{1}{1 + \Delta_{inj}/(\hbar\omega)} \left[ \frac{\sqrt{g^*\tau^*} - 1}{\sqrt{g^*\tau^*}} \right]^2 \tag{1.1}$$

where $\eta_{tr}$ is the laser transition efficiency, $\Delta_{inj}$ is the voltage defect, $g^*$ is the gain to loss cross section, and $\tau^*$ is the ratio of the upper state lifetime to the global transit time (of an electron through the active region at resonance). Therefore, the toolbox for maximizing WPE contains enhancing the values of $g^*$, $\tau^*$, and $\eta_{tr}$ while minimizing the effects of thermal

backfilling by reducing $\Delta_{inj}$.

The current state of the art for high-WPE QCL active regions in the MWIR is shown in Fig. 1.6. The first design, shown in Fig. 1.6a, is based on a shallow-well design and tall AlAs barriers [2], that measured a pulsed WPE of 31% [53], and a continuous wave WPE of 22% [54] at 4.9 $\mu$m. This design is similar to the BTC design with a diagonal transition and a narrow lower miniband in the active region. It uses five different compositions of $In_{x,y}Ga_{1-x}Al_{1-y}As$: the close-to-lattice-matched well and barrier in the active region reduce the scattering due to interface roughness, while at the same time increase the energy separation of the upper level $n = 3$ and the parasitic level $n = 4$. Additionally, the use of tall AlAs barriers in the injector region reduces the over-the-barrier leakage.

The next design, shown in Fig. 1.6b, is based on a strain-balanced $In_{0.69}Ga_{0.31}As$/ $In_{0.22}Al_{0.78}As$, that measured pulsed room temperature WPE of 28.3% at 5.6 $\mu$m [34]. This was accomplished by improving the injection efficiency and reducing the leakage to the parasitic level $n = 5$. The first thin well/barrier in 3 and 4 QW active regions is conventionally used for LWIR QCLs to suppress carrier injection from the ground level $g$ directly to the lower laser level $n = 3$. However, this is not a concern for mid-IR QCLs, and removing the first well/barrier increased the energy separation of upper level and the parasitic level $E_{54}$ by $\sim$ 20 meV, as well as reducing their spatial overlap. Although this WPE is lower than the 31% value achieved for the shallow-well design at 4.9 $\mu$m [53], the growth and commercialization of this design is perhaps more feasible due to only two compositions being used.

Finally, it is noteworthy to mention that while the intrinsic performance of a specific active region determines the WPE in pulsed mode, the thermal resistance coming from processing and mounting can make or break the WPE of the device in continuous wave mode.

## 1.4 Thesis overview

This thesis provides a detailed look into a QCL operating around 5 $\mu$m and discusses its efficiency and avenues to improve it, as well as developing a detailed fabrication process flow and characterization methods. In doing so, a reliable numerical tool is developed to simulate the bandstructure of QCLs in the semiclassical regime for both two- and multi-composition systems, with the capability of calculating the state lifetimes due to various important scattering mechanisms. This empirical rate equation model is paired with the self-consistent NEGF solver from nextnano simulation package to investigate their performance in the scattering and coherent evolution regime. Additionally, a laser operating at 20 $\mu$m is designed, fabricated, and tested. This laser exploits the metal-metal waveguide configuration used in our THz QC-lasers to lower the waveguide loss and increase confinement factor.

The thesis outline is as follows. The physics underlying the QCL operation and its theoretical modeling is provided in chapter 2, along with an explanation of various important scattering mechanisms. Chapter 3 goes over the efficiency study of a 5 $\mu$m design by comparing the rate equation model with the self-consistent NEGF method. Additionally, a detailed explanation of the QC ridge laser fabrication and characterization process is outlined. Chapter 4 describes the design, fabrication, and testing of a 20 $\mu$m QCL which is currently under further development. Conclusion is stated in Chapter 5. The detailed fabrication process flow can be found in the Appendix A, and capacitance-voltage characterization details are stated in Appendix B.

# CHAPTER 2

# Theory and Modeling

## 2.1 Introduction

In this chapter, I will discuss the theory of intersubband lasers with transitions in the conduction band, including gain and level lifetime calculations. Additionally, a numerical model for solving the electronic states in a QCL active region is discussed. Since for mid-IR QCLs, carriers acquire high levels of energy away from the subband minima of the conduction band, the non-parabolicity effects are important and cannot be ignored, and therefore they are included in the numerical bandstructure solver. Additionally, the theory described here is not unique to mid-IR QCLs, and can be used across all intersubband devices operating in the conduction band.

## 2.2 Electronic states

The recent advancements in semiconductor growth has given rise to semiconductors heterojunctions, originally proposed by Herbert Kroemer [32], which has revolutionized the field of semiconductor electronics and optoelectronics. They give us a unique ability to engineer the electronic energy bands by growing a stack of different lattice matched materials, which have enabled the growth of intersubband devices including QCLs.

The electron wavefunction in bulk semiconductors can be approximated as the vacuum free electron wavefunction with a modified electron mass due to the lattice potential, called

the electron effective mass. This is called the *effective mass approximation.* For devices where the electron is mostly in the minima of the conduction band, this mass can be approximated by a constant, such as $m^*$=0.067$m_0$ in GaAs and $m^*$=0.043$m_0$ in $In_{0.53}Ga_{0.47}As$. Although this concept was originally proposed for bulk semiconductors where the crystal is effectively infinite compared to the electron wavefunction, it can also be extended to heterojunctions with a spatially varying effective mass as long as the layers are not very thin.

In general, the electron wavefunction in a crystalline lattice is given by

$$\Psi(\mathbf{r}) = F(\mathbf{r})U_{n,0}(\mathbf{r}) \tag{2.1}$$

where $U_{n,0}(\mathbf{r})$ is the Bloch state which has the periodicity of the lattice, and $F(\mathbf{r})$ is the envelope function which is slowly varying compared to $U$. Under the *envelope function approximation* [3], the physical properties of $\Psi(\mathbf{r})$ can be deduced from the slowly varying envelope function rather than the total wavefunction which is rapidly varying on the scale of the crystal lattice. Within this approximation, the stationary Schrödinger equation becomes

$$\left[-\frac{\hbar^2\nabla_{||}^2}{2m^{||}(z)} - \frac{\hbar^2}{2}\frac{\partial}{\partial z}\frac{1}{m^*(z)}\frac{\partial}{\partial z} + E_c(z)\right] F(\mathbf{r}) = EF(\mathbf{r}) \tag{2.2}$$

where $\nabla_{||}$ and $m^{||}$ are the in-plane differential operator and effective mass, respectively. The solution for the envelope function is given by

$$F(\mathbf{r}) = \frac{1}{\sqrt{S_{||}}} e^{i\mathbf{k}_{||}\cdot\mathbf{r}_{||}} \psi_n(\mathbf{k}_{||}, z) \tag{2.3}$$

where $\psi_n(\mathbf{k}_{||}, z)$ satisfies

$$\left[-\frac{\hbar^2}{2}\frac{\partial}{\partial z}\frac{1}{m^*(z)}\frac{\partial}{\partial z} + E_n(\mathbf{k}_{||})\right] \psi_n(\mathbf{k}_{||}, z) = E_n(\mathbf{k}_{||})\psi_n(\mathbf{k}_{||}, z) \tag{2.4}$$

where $\mathbf{k}_{||}$, $n$, and $S_{||}$ are the in-plane wavevector, subband index, and normalization area, respectively, and $E_n(\mathbf{k}_{||})$ is the total energy which depends on the in-plane electron motion. This equation can be decoupled by neglecting the $z$ dependence of the in-plane effective mass $m^{||}$, which will yield the 1D Schrödinger equation

$$\left[-\frac{\hbar^2}{2}\frac{\partial}{\partial z}\frac{1}{m^*(z)}\frac{\partial}{\partial z} + E_c(z)\right] \psi_n(z) = E_n(z)\psi_n(z) \tag{2.5}$$

The neglection of the in-plane term is valid as long as the in-plane kinetic energy is not too large compared to the barrier height, and the well and barrier effective masses do not differ by much. The Eq. 2.5 is solved numerically using a finite difference method (refer to section 2.5). Additionally, space-charge effects for high-doped structures can be included by solving the Poisson equation and Eq. 2.5 iteratively. If the doping is not too high, this can be neglected, although one needs to be careful and check the validity of this assumption for a given active region.

## 2.3 Intersubband transition and gain

In this section, the gain of the QCL is derived, based on [55], which is based on the treatment in Yariv [58] and Smet [43]. Though non-parabolicity generally results in a small reduction of oscillator strength, it is ignored in the following derivation for simplicity.

The transition rate between subbands is given by Fermi's golden rule

$$W_{i \to f} = \frac{2\pi}{\hbar} \left| \left\langle f, n_{\mathbf{q},\sigma} \left| H^{'} \right| i, m_{\mathbf{q},\sigma} \right\rangle \right|^2 \delta(E_f(\mathbf{k}_f) - E_i(\mathbf{k}_i) \pm \hbar\omega_{\mathbf{q}}) \tag{2.6}$$

where the interaction Hamiltonian $H^{'}$ is given by

$$H^{'} = -\frac{e}{m^*}\mathbf{A}.\mathbf{P} \tag{2.7}$$

where $|i, m_{\mathbf{q},\sigma}\rangle$ and $|f, n_{\mathbf{q},\sigma}\rangle$ are the initial and final states with $m$ and $n$ photons in each mode given by the photon wavevector $\mathbf{q}$ at frequency $\omega_{\mathbf{q}}$ with polarization given by $\sigma = 1, 2$, and $m^*$ is the well effective mass.

The Lorentz gauge vector potential $\mathbf{A}$ for harmonic interaction is given by

$$\mathbf{A} = \sqrt{\frac{\hbar}{2\epsilon\omega_{\mathbf{q}}V}}\hat{\mathbf{e}}_{\mathbf{q},\sigma}[a_{\mathbf{q},\sigma}e^{i\mathbf{q}\cdot\mathbf{r}} + a^{\dagger}_{\mathbf{q},\sigma}e^{-i\mathbf{q}\cdot\mathbf{r}}] \tag{2.8}$$

where $\epsilon$, $V$, and $\hat{\mathbf{e}}_{\mathbf{q},\sigma}$ are the permittivity, volume of the cavity, and the polarization vector

respectively. The matrix element is then given by

$$\begin{aligned} |\langle H'_{i\to f}\rangle|^2/C = & m_{\mathbf{q},\sigma}\delta_{m_{\mathbf{q},\sigma}-1,n_{\mathbf{q},\sigma}} \left|\left\langle f \left| e^{i\mathbf{q}.r}\hat{\mathbf{e}}_{\mathbf{q},\sigma}.\mathbf{p}\right| i\right\rangle\right|^2 \\ & + (m_{\mathbf{q},\sigma}+1)\delta_{m_{\mathbf{q},\sigma}+1,n_{\mathbf{q},\sigma}} \left|\left\langle f \left| e^{-i\mathbf{q}.r}\hat{\mathbf{e}}_{\mathbf{q},\sigma}.\mathbf{p}\right| i\right\rangle\right|^2 \end{aligned} \tag{2.9}$$

$$C = \frac{e^2\hbar}{2m^{*2}\epsilon\omega_{\mathbf{q}}V} \tag{2.10}$$

where the first and second terms in Eq. 2.9 correspond to absorption and emission respectively, and the term proportional to $m_{\mathbf{q},\sigma}$ in the second term corresponds to stimulated emission while the field independent term corresponds to spontaneous emission.

We can write the initial and final states in the real space basis by projecting them onto the position operator as follows

$$\langle \mathbf{r}|i\rangle = \frac{1}{\sqrt{S_{||}}}e^{i\mathbf{k}_{||,i}.\mathbf{r}_{||}}\psi_i(z) \tag{2.11}$$

$$\langle \mathbf{r}|f\rangle = \frac{1}{\sqrt{S_{||}}}e^{i\mathbf{k}_{||,f}.\mathbf{r}_{||}}\psi_f(z) \tag{2.12}$$

where $S_{||}$ is the normalization factor. Since we are in the optical regime, we can adopt the electric dipole approximation $e^{i\mathbf{q}.r} \cong 1$. Therefore

$$\begin{aligned} \left\langle f \left| e^{\pm i\mathbf{q}.\mathbf{r}}\hat{\mathbf{e}}_{\mathbf{q},\sigma}.\mathbf{p}\right| i\right\rangle & \cong \langle f \left|\hat{\mathbf{e}}_{\mathbf{q},\sigma}.\mathbf{p}\right| i\rangle \\ & = [\hat{\mathbf{e}}_{\mathbf{q},\sigma}.\mathbf{k}_{||,i}]\frac{\hbar}{S_{xy}}\int d\mathbf{r}_{||}e^{i(\mathbf{k}_{||,i}-\mathbf{k}_{||,f}).\mathbf{r}_{||}}\int dz\psi_f^*(\mathbf{k}_{||,f},z)\psi_i(\mathbf{k}_{||,i},z) \\ & \quad - \hat{\mathbf{z}}\frac{i\hbar}{S_{xy}}\int d\mathbf{r}_{||}e^{i(\mathbf{k}_{||,i}-\mathbf{k}_{||,f}).\mathbf{r}_{||}}\int dz\psi_f^*(\mathbf{k}_{||,f},z)\frac{\partial\psi_i(\mathbf{k}_{||,i},z)}{\partial z} \\ & = [\hat{\mathbf{e}}_{\mathbf{q},\sigma}.\hat{\mathbf{z}}]\delta_{\mathbf{k}_{||,f},\mathbf{k}_{||,i}}\langle\psi_f\left|p_z\right|\psi_i\rangle \end{aligned} \tag{2.13}$$

where the first term in the subtraction is zero due to the wavefunction orthonormality, which is also known as the intersubband selection rule.

Given the commutation relation

$$\frac{i}{\hbar}[H_0,z] = \frac{p_z}{m^*} \tag{2.14}$$

we arrive at

$$\langle f\,|p_z|\,i\rangle = \frac{im^*}{\hbar}(E_f - E_i)\,\langle\psi_f\,|p_z|\,\psi_i\rangle \tag{2.15}$$

where $\langle\psi_f\,|p_z|\,\psi_i\rangle$ is the dipole matrix element of the transition. We can then arrive at the following transition rates for spontaneous and stimulated emission

$$W^{(sp)}_{i\to f/mode} = \frac{\pi e^2\omega_{\mathbf{q}}}{\epsilon V}|\hat{\mathbf{e}}_{\mathbf{q},\sigma}.\hat{\mathbf{z}}|^2|z_{i\to f}|^2\delta(E_f - E_i + \hbar\omega_{\mathbf{q}}), \tag{2.16}$$

$$W^{(st)}_{i\to f/mode} = \frac{\pi e^2\omega_{\mathbf{q}}}{\epsilon V}|\hat{\mathbf{e}}_{\mathbf{q},\sigma}.\hat{\mathbf{z}}|^2|z_{i\to f}|^2\delta(E_f - E_i + \hbar\omega_{\mathbf{q}})m_{\mathbf{q}.\sigma} \tag{2.17}$$

where $m_{\mathbf{q}.\sigma}$ is the number of photons with wavevector $\mathbf{q}$ in the polarization mode $\sigma$. Next, we can sum 2.16 over all photon modes and polarizations in the cavity to obtain

$$W^{(sp)}_{i\to f} = \frac{e^2 n\omega_0^3}{3\pi\epsilon_0\hbar c^3}|z_{i\to f}|^2 = \frac{e^2 n\omega_0^2}{6\pi m^*\epsilon_0 c^3}f_{i\to f} \tag{2.18}$$

where $n$, $\omega_0$, and $c$ are the index of refraction, frequency, and speed of light. The scaled oscillator strength is given by

$$f_{i\to f} = \frac{m^*}{m_0}f_{i\to f,unscaled} = \frac{2m^*(E_f - E_i)|z_{i\to f}|^2}{\hbar^2} \tag{2.19}$$

This is true when non-parabolicity is negligible. If non-parabolicity is not small, then the oscillator strength can be defined in terms of the momentum matrix elements as [41]

$$f_{i\to f} = \frac{2}{m_0}\frac{|\langle\psi_f\,|p_z|\,\psi_i\rangle|^2}{E_i - E_f} \tag{2.20}$$

where the effective mass is included in the expectation value. Then the matrix element can be written in terms of the conduction band component as [41]

$$\langle\psi_f\,|p_z|\,\psi_i\rangle = \frac{i\hbar}{2}\int\left[\frac{m_0}{m^*(z,E_f)}\frac{d\psi_f(z)}{dz}\psi_i(z) - \frac{m_0}{m^*(z,E_i)}\psi_f^*(z)\frac{d\psi_i(z)}{dz}\right]dz \tag{2.21}$$

which generally results in slightly smaller oscillator strength values than the parabolic case.

To calculate the rate of the stimulated emission, the Eq. 2.17 is integrated over all electromagnetic modes to get the total stimulated emission rate as

$$W^{(st)}_{i\to f} = 3\times W^{(sp)}_{i\to f}.m_{\mathbf{q},\sigma}.g(\nu) = \frac{3\lambda^2}{8\pi n^2 h\nu\tau^{(sp)}_{i\to f}}I(\nu)g(\nu) \tag{2.22}$$

where the $\times 3$ factor is due to all electron dipoles being in the $z$ direction, which is the same as the polarization of the incident field. Also, the Dirac-deta function is replaced with the normalized lineshape function $g(\nu)$ as the energy levels are broadened due to having finite lifetime. The lineshape function is given by

$$g(\nu) = \frac{(\Delta\nu/2\pi)}{(\nu - \nu_0)^2 + (\Delta\nu/2)^2} \tag{2.23}$$

where

$$\Delta\nu = \frac{1}{\pi}\left(\frac{1}{2\tau_i} + \frac{1}{2\tau_f} + \frac{1}{T_2^*}\right) \tag{2.24}$$

is the FWHM linewidh of the transition, and $T_2^*$ is the pure dephasing time.

Now using the expressions for the spontaneous and stimulated emission, we can derive the optical gain. Assuming a two level system with $N_2W_{21}$ representing the induced transitions from 2→1, and $N_1W_{12}$ the induced transitions from 1→2, the small signal gain for a transition with population inversion of $\Delta N$ per unit volume is given by

$$\begin{aligned} g(\nu) &= \frac{\Delta N e^2 \pi \nu_0 |z_{i\to f}|^2}{\hbar c n \epsilon_0} g(\nu) \\ &= \frac{\Delta N e^2 f_{i\to f}}{4m^* c n \epsilon_0} g(\nu) \end{aligned} \tag{2.25}$$

where the unit for gain expressed here is per unit length.

## 2.4 Scattering mechanisms and level lifetime

Transport and gain in QCLs occur due to scattering events, which are transition of carriers from one subband to another due to a non-constant potential, which is usually treated using perturbation theory. These events are further responsible for the population inversion between levels which provides the gain of the QCL. There are two main types of scattering mechanisms: inter- and intra- subband scattering, which is scattering of a carrier between subbands and within the same subband, respectively. These scattering events are summarized in Fig. 2.1. Elastic scattering happens for time constant potentials, and the carrier

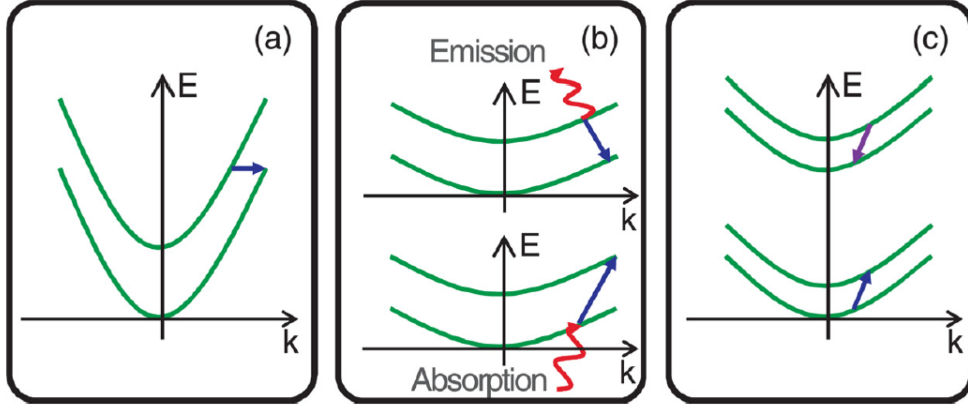


Figure 2.1: Different classes of scattering processes: (a) elastic scattering; (b) inelastic scattering; (c) carrier-carrier scattering; from Ref. [23].

energy is conserved after the scattering event. Some examples of this type of scattering are impurity, interface roughness, and alloy disorder scattering. An especially important type of scattering is the inelastic scattering where the potential has a time-harmonic dependence with a frequency $\omega_0$. Longitudinal optical (LO) phonons are an important example of this type of scattering. The carrier energy after the scattering event is not preserved, and it is either increased (absorption of $\hbar\omega_0$) or decreased (emission of $\hbar\omega_0$). The last type of scattering is a special case of intercarrier scattering, such as electron-electron scattering. In the following sections, I will discuss some of the important scattering mechanisms including a brief derivation of their scattering rates.

### 2.4.1 LO phonon scattering

Longitudinal optical (LO) phonons are a prominent scattering mechanism in III-V semiconductors, which provide an efficient way for carriers to cool down. This scattering mechanism can be beneficial in extracting carriers efficiently from the lower level by placing the injector levels an $E_{LO}$ below the lower laser level (called resonant-phonon depopulation), and in cooling the hot electrons in the injector region. On the other hand, the LO phonon can be

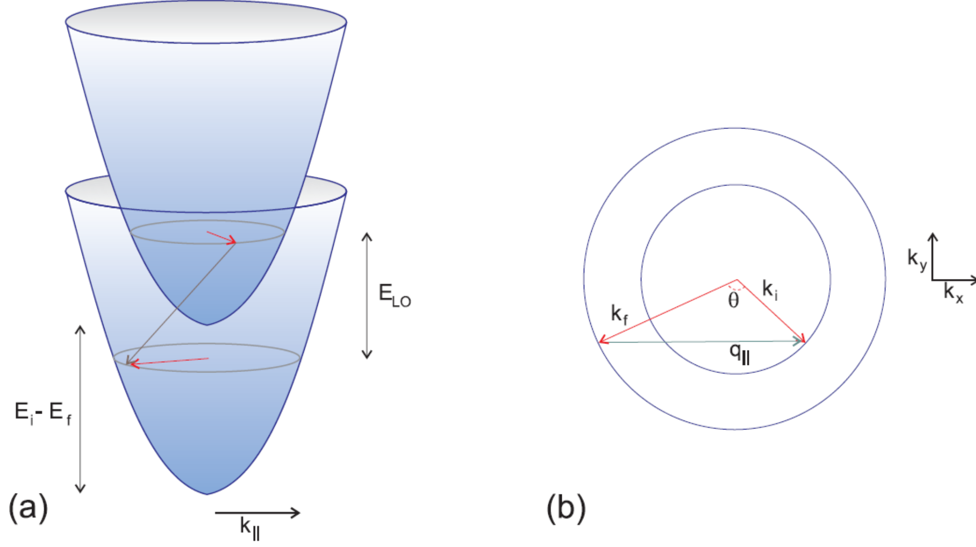


Figure 2.2: (a) Schematic illustration of intersubband LO-phonon scattering process. (b) In-plane reciprocal lattice space diagram illustrating the relationship between initial and final electron wavevectors $k_i$ and $k_f$ and in-plane phonon wavevector $q_{||}$, from Ref. [55].

detrimental to the QCL operation, such as LO phonon absorption of carriers in the upper laser level into the parasitic channels, or direct depopulation from the high energy tail of the upper laser subband into the lower laser level. The following derivation is based on Ref. [55]. In the derivation, the phonon spectrum is taken as the bulk spectrum of the well material (InGaAs), which is a reasonable assumption to calculate the LO lifetime and understand the transport. The optical phonon branch is assumed to be dispersionless, and $E_{LO} = 34$ meV is assumed for InGaAs. The scattering rate from an initial state $|i, \mathbf{k}_i\rangle$ (subband $i$, in-plane wavevector $\mathbf{k}_i$) to the final state $|f, \mathbf{k}_f\rangle$ is given by Fermi's golden rule

$$W_{i\to f}(\mathbf{k}_i, \mathbf{k}_f) = \frac{2\pi}{\hbar} \left| \left\langle f, \mathbf{k}_f \left| H' \right| i, \mathbf{k}_i \right\rangle \right|^2 \delta(E_f(\mathbf{k}_f) - E_i(\mathbf{k}_i) \pm \hbar\omega_{LO}) \tag{2.26}$$

Where the electron-phonon interaction Hamiltonian is

$$H' = \sum_{\mathbf{q}} [\alpha(\mathbf{q})(e^{i\mathbf{q}\cdot\mathbf{r}} b_{\mathbf{q}} + e^{-i\mathbf{q}\cdot\mathbf{r}} b^{\dagger}_{\mathbf{q}})] \tag{2.27}$$

where $\alpha(\mathbf{q})$ is the electron-phonon interaction and $b_{\mathbf{q}}$ and $b_{\mathbf{q}}^{\dagger}$ are the creation and annihilation operators for a phonon in mode $\mathbf{q}$. The Fröhlich interaction strength for electron-polar-optical-phonon is given by

$$|\alpha(\mathbf{q})|^2 = \frac{\hbar\omega_{LO}}{2}\frac{e^2}{q^2}\left(\frac{1}{\epsilon_\infty} - \frac{1}{\epsilon_{dc}}\right) \tag{2.28}$$

where $\epsilon_{dc}$ and $\epsilon_\infty$ are the static and high frequency permittivities. Note that scattering between subbands with a large energy separation is weaker due to the $q^{-2}$ dependence. The matrix element is given by

$$\begin{aligned} \left|\left\langle f, \mathbf{k}_f \left| H^{'} \right| i, \mathbf{k}_i \right\rangle\right|^2 = \frac{e^2\hbar\omega_{LO}}{2V}\left(\frac{1}{\epsilon_\infty} - \frac{1}{\epsilon_{dc}}\right)\frac{1}{q_z^2 + q_{||}^2}|A_{i\to f}(q_z)|^2 \\ \times\, \delta_{\mathbf{k}_i, \mathbf{k}_f \mp \mathbf{q}_{||}}(n_{\omega_{LO}} + 1/2 \mp 1/2) \end{aligned} \tag{2.29}$$

where $\mathbf{q}_{||}$, $\mathbf{q}_z$, and $n_{\omega_{LO}}$ are the in-plane and parallel to growth axis phonon wavevector components, and the Bose-Einstein occupation, respectively. Also, the upper and lower signs correspond to the phonon absorption and emission respectively. The form factor $A$ is given by

$$A_{i\to f}(q_z) = \int_{-\infty}^{\infty} dz \psi_f^*(z)\psi_i^* z e^{\pm q_z z} \tag{2.30}$$

After summing over the phonon modes $\mathbf{q}$, the Eq. 2.26 can be integrated over the final states $\mathbf{k}_f$ to get the total scattering rate from the initial wavevector $\mathbf{k}_i$:

$$\begin{aligned} W_{i\to f}^{abs}(\mathbf{k}_i) &= \frac{m^* e^2\omega_{LO}}{8\pi\hbar^2}\left(\frac{1}{\epsilon_\infty} - \frac{1}{\epsilon_{dc}}\right) n_{\omega LO}\int_0^{2\pi} d\theta B_{i\to f}(q_{||}) \\ W_{i\to f}^{em}(\mathbf{k}_i) &= \frac{m^* e^2\omega_{LO}}{8\pi\hbar^2}\left(\frac{1}{\epsilon_\infty} - \frac{1}{\epsilon_{dc}}\right)(n_{\omega LO} + 1)\int_0^{2\pi} d\theta B_{i\to f}(q_{||}) \end{aligned} \tag{2.31}$$

where $B_{i\to f}$ is given by

$$B_{i\to f} = \int_{-\infty}^{\infty} dz \int_{-\infty}^{\infty} dz^{'} \psi_f^*(z)\psi_i(z)\psi_i^*(z^{'})\psi_f^*(z^{'})\frac{1}{q_{||}}e^{-q_{||}|z-z^{'}|} \tag{2.32}$$

Then the total scattering time between subbands $i \to f$, as shown in Fig. 2.2, is obtained by averaging over all initial states as

$$\frac{1}{\tau_{i\to f}} = \frac{\int_0^\infty dE_k f_i[E_k] W_{i\to f}(E_k)}{\int_0^\infty dE_k f[E_k]} \tag{2.33}$$

where $E_k = \hbar^2 k_{||}^2/2m^*$ is the in-plane kinetic energy in the initial subband, and $f_i[E_k]$ is the corresponding Fermi function.

### 2.4.2 Interface roughness scattering

In addition to LO phonon scattering, it has been shown that interface roughness scattering (IFR) is also an important scattering mechanism, especially for mid-IR QCLs, and can effect both EL linewidths and carrier lifetimes [8, 56]. The model used to find the linewidth for interface roughness is based on the theory of Ando et.al [1] and Unuma et.al [48, 49]. We assume an uncorrelated interface and a standard Gaussian autocorrelation of roughness given by

$$\left\langle h(r_{||})h(r_{||}^{'})\right\rangle = \Delta^2 exp(-|r_{||} - r_{||}^{'}|^2/\Lambda^2) \tag{2.34}$$

where $\Delta$ and $\Lambda$ are the average roughness height and the correlation length, respectively. These parameters are obtained by comparing the experimentally obtained EL to the calculated one, where the FWHM of individual IFR-induced inhomogeneous broadening between levels are given by [56, 31]

$$2\gamma_{ul,ll}^{IFR} = \frac{\pi}{\hbar^2}\Delta^2\Lambda^2\sum_i m_i^*\Delta_{CB,i}^2\left(\psi_{ul}^2(z_i) - \psi_{ll}^2(z_i)\right)^2 \tag{2.35}$$

where $m_i^*$ and $\Delta_{CB,i}$ are the electron effective mass and the conduction band offset at the $i^{th}$ interface, and $\psi_{ul,ll}(z_i)$ are the wavefunction amplitudes of the upper and lower levels at the $i^{th}$ interface. Then using the extracted parameters, the IFR-induced intersubband scattering is then calculated as [8]

$$\frac{1}{\tau_{m,n}^{IFR}} = \frac{\pi}{\hbar^3}\Delta^2\Lambda^2\sum_i m_i^*\Delta_{CB,i}^2\psi_m^2(z_i)\psi_n^2(z_i)\exp\left(-\frac{\Lambda^2 m_i^* E_{mn}}{2\hbar^2}\right) \tag{2.36}$$

where $m$ and $n$ represent the indices of the initial and final states, and $E_{mn}$ is the energy spacing between the states. It can be seen from Eq. 2.36 that the IFR lifetime is inversely proportional to the square of the conduction band offset at the interface, and exponentially decreases as the energy separation between the states gets smaller. Thus, these can be used as design parameters to either increase or decrease IFR during the design stage.

### 2.4.3 Alloy disorder scattering

Assuming that the dopants are placed in the injector region away from the active part of the module such that impurity scattering is minimized, the next important scattering mechanism is alloy disorder scattering (AD). Although it does not affect the EL linewidth, AD can account for up to 70% of the total elastic scattering for lattice matched structures [50]. The expression for alloy disorder scattering lifetime is given by [38], which is based on the theory of [49, 50]. For a ternary semiconductor of type $A_xB_{1-x}C$, the scattering Hamiltonian is given by

$$H_{alloy} = \Delta E_C \delta x(r) \tag{2.37}$$

where $\Delta E_C$ if the conduction band minima difference of AC and BC, and $\Delta x(r)$ is the concentration fluctuation which is given by the correlation function

$$\left\langle \Delta x(r)\Delta x(r^{'}) \right\rangle = \frac{a^2}{4} x(1-x)\Delta(r-r^{'}) \tag{2.38}$$

where $a$ is the lattice constant. The scattering matrix element for AD is given by [49]

$$\left| \left\langle j\mathbf{k}^{'}|H_{alloy}|i\mathbf{k} \right\rangle \right| = \frac{a^3(\Delta E_C)^2 x(1-x)}{4} \int_{alloy} \psi_i^2(z)\psi_j^2(z)dz \tag{2.39}$$

Note that there is no energy dependence in the scattering matrix element, and a spatial overlap of the wavefunctions is sufficient for short AD scattering time. Also, assuming constant spatial overlap, the matrix element is maximized for $x$=0.5 and vanishes for Binary alloys, i.e, $x$=0 or 1. The AD lifetime is then given by [46, 50]

$$\frac{1}{\tau_{ij}^{inter,AD}} = \frac{1}{8}\frac{m_i^* a^3(\Delta E_C)^2 x(1-x)}{\pi\hbar^3} \int_{alloy} \psi_i^2(z)\psi_j^2(z)dz \tag{2.40}$$

where $i$,$j$ are the initial and final states respectively, $m_i^*$ is the effective mass of the well or barrier, and $x$ is the mole fraction of the ternary compounds $In_{1-x}Ga_xAs$ or $Al_xIn_{1-x}As$.

## 2.5 Schrödinger solver

The first step in designing the active region of a QCL is solving for the quasi-bound subband states. They determine important properties of the QCL, such as the upper and lower lasing level separation, i.e the lasing frequency, the coupling strength between the injector and the upper level, and the injector level spacing from the lower laser level. Additionally, the radiative and nonradiative scattering rates between states is crucial in determining the level lifetimes and gain of the QCL, and they depend on the accurate knowledge of the electronic wavefunctions. Due to the uncertainty in material parameters such as conduction band offset and electron effective mass, the measurements deviate from design in most cases. Therefore, a robust and computationally efficient numerical modeling is essential to ensure adequate turnaround time in the design, fabrication, and characterization processes. To do so, the eigenvalues and eigenstates of the Hamiltonian is determined by solving the Schrödinger equation using a numerical method.

### 2.5.1 Shooting method

In numerical analysis, the shooting method is a method for solving a boundary value problem by reducing it to a system of initial value problem [20]. Roughly speaking, we “shoot” out trajectories in different directions until we find a trajectory that has the desired boundary value, as shown in Fig. 2.3. The time independent Schrödinger equation is given by

$$\frac{-\hbar^2}{2m^*}\frac{\partial^2}{\partial z^2}\psi(z) + V(z)\psi(z) = E\psi(z) \tag{2.41}$$

Where $\hbar$, $m^*$, $E$, and $V(z)$ are the Planck's constant, effective mass, energy, and the potential, respectively. This equation is exactly solvable for a handful of potentials, such as the free particle, infinite potential well, and quantum harmonic oscillator. However, for most problems, including QCLs, the solution to the Schrödinger equation is approximated using numerical methods.

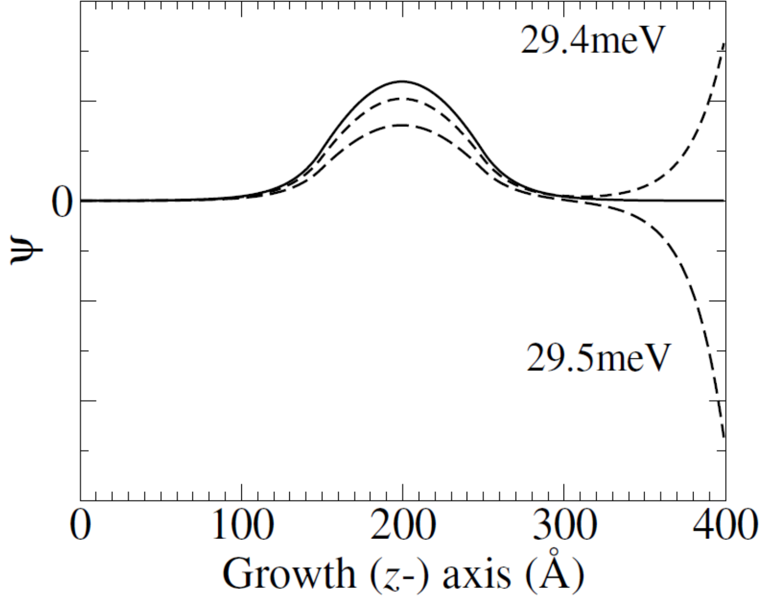


Figure 2.3: Numerically obtained wavefunctions above and below the true solution at E = 29.43 meV, for an electron in a 150°A $Ga_{0.8}Al_{0.2}As$/100°A GaAs/150°A $Ga_{0.8}Al_{0.2}As$ single quantum well, from Ref. [20].

In the shooting method, the Schrödinger equation is solved using a finite difference method, where a spatial grid of spacing $\delta z$ is defined for $\psi(z)$, $V(z)$, and $m^*(z)$, and the partial derivative terms are expanded using their limit definitions as follows

$$\frac{d}{dz}f \approx \frac{f(z+\delta z) - f(z-\delta z)}{2\delta z} \tag{2.42}$$

$$\frac{d^2}{dz^2}f \approx \frac{f(z+\delta z) - 2f(z) + f(z-\delta z)}{\delta z^2} \tag{2.43}$$

Then, using 2.42-2.43, we can rewrite 2.41,

$$\psi(z+\delta z) = \left[\frac{2m^*}{\hbar^2}\delta z^2[V(z) - E] + 2\right]\psi(z) - \psi(z-\delta z) \tag{2.44}$$

This implies that if the wavefunction is known at points $(z - \delta z)$ and $z$, then the value of the wavefunction at $(z + \delta z)$ can be calculated for any energy $E$. This iterative equation

forms the basis of a standard method for solving differential equations numerically, and it is known as the shooting method.

The solutions for the stationary states have wavefunctions which satisfy the standard boundary conditions, i.e.

$$\psi(z) \to 0 \quad \text{and} \quad \frac{\partial}{\partial z}\psi(z) \to 0 \quad \text{as} \quad z \to \pm\infty \tag{2.45}$$

To start the iteration, the first two values of the wavefunction can be chosen as 0 and 1 since the eigenvalues of the Schrödinger equation are unchanged if the wavefunction is scaled by a number,

$$\psi(0) = 0, \qquad \psi(\delta z) = 1 \tag{2.46}$$

Then the solution to the equation $\psi(\infty, E) = 0$ is sought using an iterative method such as the Newton-Raphson method.

For the case of dissimilar effective masses between junctions, the Schrödinger equation and boundary conditions need to be slightly modified as a consequence of requiring the kinetic energy operator to be Hermitian, thus:

$$\frac{-\hbar^2}{2m^*}\frac{\partial^2}{\partial z^2} \quad \text{needs to be transformed into} \quad \frac{-\hbar^2}{2}\frac{\partial}{\partial z}\left(\frac{1}{m^*(z)}\frac{\partial}{\partial z}\right) \tag{2.47}$$

And the standard boundary conditions get modified to the BenDaniel-Duke [5] boundary conditions as:

$$\psi(z) \to 0 \quad \text{and} \quad \frac{1}{m^*}\frac{\partial}{\partial z}\psi(z) \to 0 \quad \text{as} \quad z \to \pm\infty \tag{2.48}$$

Therefore, rewriting the Schrödinger equation using the modified form of the momentum operator and expanding the derivative terms as before, we arrive at the following iterative relation for the Schrödinger equation with varying masses:

$$\frac{\psi(z+\delta z)}{m^*(z+\delta z/2)} = \left[\frac{2}{\hbar^2}\delta z^2[V(z)-E] + \frac{1}{m^*(z+\delta z/2)} + \frac{1}{m^*(z-\delta z/2)}\right]\psi(z) - \frac{\psi(z-\delta z)}{m^*(z-\delta z/2)} \tag{2.49}$$

### 2.5.2 Nonparabolicity

The constant effective mass approximation, which assumes a parabolic subband, breaks down for high kinetic energy electrons that move away from the $k = 0$. This makes the effective mass both spatial and energy dependent, $m(z, E)$, and ignoring this can cause a considerable error in the eigenenergies. This is especially important in mid-IR QCLs since the energy scales are larger than that of THz QCLs, and electrons acquire higher temperatures and move away from Γ-valley into the nonparabolic parts of the band dispersion.

We use the Kane model [27] to incorporate the nonparabolicity into the bandstructure calculation. For conduction band states, the general Hamiltonian is a 8×8 matrix which includes conduction, light holes, heavy holes, and split-off holes states ×2 for spin. This can be reduced to a 4×4 matrix if spin-orbit coupling is weak, and then further reduce to a 3×3 matrix for decoupled heavy holes [41] as follows,

$$H = \begin{pmatrix} E_c(\mathrm{z}) & \sqrt{2}\alpha & -\alpha \\ \sqrt{2}\alpha^* & E_{lh} & 0 \\ -\alpha^* & 0 & E_{so} \end{pmatrix}, \qquad \psi = \begin{pmatrix} C \\ L \\ S \end{pmatrix} \tag{2.50}$$

where $E_c$, $E_{lh}$, and $E_{so}$ are the conduction band, light hole, and split-off bands, and $\alpha = ip_z\sqrt{\frac{E_p}{6m_0}}$ where $E_p$ is the Kane energy which is material dependent. Solving for the light-hole and split-off components and plugging into the conduction component of 2.50 gives the following Schrödinger equation with energy dependent effective mass,

$$\frac{-\hbar^2}{2m_0}\frac{\partial}{\partial z}\left[\frac{2}{3}\frac{E_p}{E - E_{lh}} + \frac{1}{3}\frac{E_p}{E - E_{so}}\right]\frac{\partial}{\partial z}C + E_cC = EC \tag{2.51}$$

with the effective mass given as,

$$\frac{m_0}{m^*(E, z)} = \frac{2}{3}\frac{E_p}{E - E_{lh}} + \frac{1}{3}\frac{E_p}{E - E_{so}} \tag{2.52}$$

This energy dependent effective mass is incorporated in the iterative shooting method to solve for $C$, and then the $L$ and $S$ components are solved for.

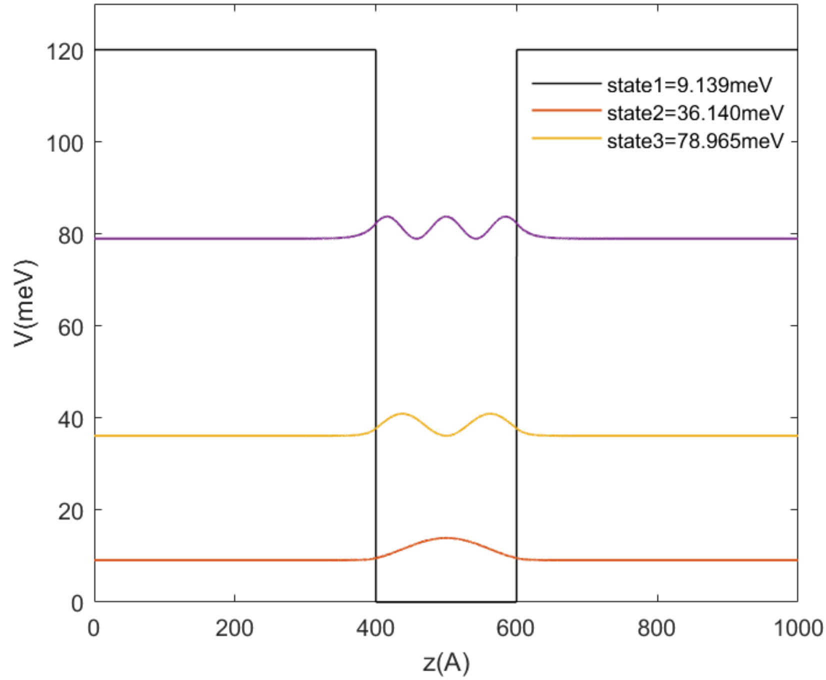


Figure 2.4: Simulated bandstructure for GaAs/$Al_{0.15}$GaAs single finite quantum well using shooting method.

### 2.5.3 Single quantum well solution

To confirm the accuracy of the implemented shooting method, the eigenenergies of a single finite quantum well with $\Delta_{CB}$=120 meV is calculated both theoretically and then using the shooting method. The barrier is $Al_{0.15}$GaAs with $m^*$=0.0795 with width of 400 nm, and well material is GaAs with $m^*$=0.067 and width of 200 nm. The simulated bandstructure is shown in Fig. 2.4, and the comparison between the theoretical and simulated eigenvalues is shown in Table 2.1. In this calculation, the nonparabolicity is ignored to make the theoretical calculation simpler.

As shown in table 2.1, the values are in close agreement which validates the accuracy of the implemented Schrödinger solver.

The analytical solution to the 1D single finite quantum well is done as follows. Solving

| Eigenenergy | $E_n$ Theoretical (meV) | $E_n$ using SM (meV) | $\Delta E_n$ (meV) |
|---|---|---|---|
| $E_1$ | 9.139 | 9.139 | 0 |
| $E_2$ | 36.140 | 36.140 | 0 |
| $E_3$ | 78.966 | 78.965 | 0.001 |

Table 2.1: Theoretical versus simulated values for the eigenenergies of single finite quantum well.

the Schrödinger equation with the given potential well, the general solution can be written piecewise as,

$$\begin{aligned} \psi(z) &= B \exp \kappa z, & z \leq \frac{-l_w}{2} \\ \psi(z) &= A \exp k z, & \frac{-l_w}{2} < z \leq \frac{l_w}{2} \\ \psi(z) &= B \exp -\kappa z, & z > \frac{l_w}{2} \end{aligned} \tag{2.53}$$

where,

$$k = \frac{\sqrt{2m_w^* E}}{\hbar}, \qquad \kappa = \frac{\sqrt{2m_b^*(V-E)}}{\hbar} \tag{2.54}$$

Then using the BenDaniel-Duke boundary condition, we arrive at the equation for the even and odd parity,

$$\begin{aligned} k \tan\left(\frac{k l_w}{2}\right) - \kappa = 0 \quad &\rightarrow \quad \text{Odd parity} \\ k \cot\left(\frac{k l_w}{2}\right) + \kappa = 0 \quad &\rightarrow \quad \text{Even parity} \end{aligned} \tag{2.55}$$

Which can be solved numerically to find the eigenenergies that satisfy these equations.

# CHAPTER 3

# MWIR QCL: design, fabrication, characterization

## 3.1 Introduction

Although the QCLs in the mid-IR region have seen an immense improvement in power levels and efficiency since their advent, they are still far from reaching their theoretical maximum levels. Given that their active regions are typically longer and contain more wavefunctions than a typical THz QCL active region, and that the energy spacing between state are typically much larger than THz ones, coherence effects and dephasing mechanisms are typically not included in their modelling. However, it could prove insightful to investigate their transport based on the powerful, yet computationally demanding, NEGF modelling which accounts for both coherent and incoherent evolution.

In this chapter, I will give a brief overview on WPE and the NEGF transport modeling method. Then I will discuss our effort in increasing the efficiency of a 5 $\mu$m QCL using both a conventional semiclassical model and the commercial nextnano.NEGF package. Additionally, a detailed fabrication process flow is presented for making ridge lasers, which I developed in support of our mid-IR Vertical-External-Cavity Surface-Emitting Laser (VECSEL) project and has been used a few times to successfully fabricate and test ridge lasers. Finally, characterization methods are developed for testing the QC-lasers characteristics, such as light-current-voltage plots, spectra and electroluminescence measurements using step-scan of FTIR.

### 3.1.1 Wall plug efficiency

There has been a continued effort in increasing the efficiency of mid-IR QCLs ever since their advent. Specifically, the wall-plug-efficiency (WPE) is the key parameter that will determine if the device is suitable for practical applications where laser cooling and supply power is limited, such as handheld devices. Simply put, the WPE is the electrical to optical power conversion efficiency,

$$\eta_w = \frac{P}{IV} \tag{3.1}$$

Where $P$, $I$, and $V$ denote the optical output power, operating current, and voltage values. The theoretical derivation of WPE is straightforward [39]. Assuming a linear relation between $P$ and $I$ above threshold (valid for pulsed), the output power can be written as

$$P = \eta_s(I - I_{th}) \tag{3.2}$$

where $\eta_s$ and $I_{th}$ are slope efficiency and threshold current density respectively. Then one can write slope efficiency as

$$P = \eta_i \frac{N\hbar\omega}{e} \frac{\alpha_m}{\alpha_m + \alpha_w} \tag{3.3}$$

where $\eta_i$, $N$, $\hbar\omega$, $e$, $\alpha_m$, $\alpha_w$ denote internal efficiency, number of QCL stages, photon energy, electron charge, mirror and waveguide loss, respectively. Then, also assuming a linear relation for IV above threshold, one can write $V$ as

$$V = V_{th} + (I - I_{th})R \tag{3.4}$$

where the $V_{th}$ and $R$ denote threshold voltage and differential resistance, respectively. Using Eq. 3.1-3.4, the wall plug efficiency can be written as the product of four sub-efficiencies: internal efficiency ($\eta_i$), optical efficiency ($\eta_0$), voltage efficiency ($\eta_V$), and electrical efficiency ($\eta_e$)

$$\eta_w = \eta_i \eta_0 \eta_v \eta_e \tag{3.5}$$

where a constant internal quantum efficiency and differential resistance is assumed, and the sub-efficiencies are

$$\eta_0 = \frac{\alpha_m}{\alpha_m + \alpha_w} \tag{3.6}$$

$$\eta_v = \frac{N\hbar\omega}{e}\frac{1}{V_{th}} \tag{3.7}$$

$$\eta_e = \frac{I - I_{th}}{I(1 + R(I - I_{th})/V_{th})} \tag{3.8}$$

The WPE efficiency parameter is not straightforward to maximize, since it is the product of four other efficiencies. Unfortunately, there is not a single strategy that one could take that would maximize all these efficiencies at the same time, and there are generally trade-offs that one needs to account for. Maximizing the QCL efficiency can be done both during the design phase (active region and waveguide design) and testing.

Some factors that one can consider during the active region design are: 1) minimizing leakage channels, including over the barrier leakage, 2) maximizing the effective lifetime of the laser $\tau_{eff}$=$\tau_3$(1-$\tau_2/\tau_{32}$), 3) minimizing voltage defect ($\Delta_{inj}$) while also keeping it sufficiently large such that the thermal backfilling from the ground state is minimized, and 4) optimizing the sheet doping density, both in terms of value and position within the module.

After designing the active region, the waveguide can be optimized such that the waveguide loss is minimized for a particular mode of interest. The thickness of the active region and cladding layers, doping of the cladding layers, and type of dielectric for insulation can all be factors that can affect the waveguide loss. Assuming the fabrication is done perfectly and with minimal defects, the metal contact and mounting techniques can also affect the WPE. For instance, Ti/Au contact has been shown to be Schottky for low doped InP substrate ($1\times10^{17}$ cm$^{-3}$ or lower), while an alloyed Ge/Au/Ni/Au contact is ohmic. And such a subtle change can result in WPE improvement inasmuch as 13% [39]. Mounting a device can also greatly affect its performance by means of efficient heat extraction. Some general techniques have been InP overgrowth after etching the ridges, and mounting epi-side down on an diamond heat spreader.

Concerning active region design, there has been two main routes for maximizing WPE through bandstructure engineering; first includes using two materials ($In_xGa_{1-x}As$ and $In_yGa_{1-y}As$) with a fixed $x$ and $y$, and second, using a multi-material system where more than one composition is used for either the well, barrier, or both. The second method provides the flexibility to have better control over the electron wavefunction, matrix elements, and scattering times. However, it comes with the downside of making the growth extremely complicated, as most MBE growth systems are configured to grow two alternating active region material. Thus, the growth complexity can potentially hinder its commercialization. Additionally, the inherent strain of the lattice mismatched materials still puts a constraint on how freely one can change the layer composition and thicknesses.

### 3.1.2 Non-equilibrium Green's Function

The Non-equilibrium Green's function (NEGF), originally introduced by Kadanoff and Baym [26] and Keldysh [30], is the most general way of modeling quantum transport in electronic and optoelectronic devices, since it includes both coherent transport effects such as resonant tunneling, and incoherent evolution such as scattering mechanisms. Since its formalism, it has been applied to various transport problems for different materials such as metals [7], semiconductors [6], topological insulators [21], and more. Their application to the transport in QCLs was first shown by Wacker [51], and has been used since then in the QCL community [52, 17, 18].

While a complete description of the NEGF formalism is beyond the scope of this thesis, I summarize here the key features of this technique. The NEGF model describes the transport with the electronic retarded and lesser Green's function $G^R$ and $G^<$ respectively [23]. Then a set of four coupled partial differential equations is formed

$$G^R = \frac{1}{E - H_0 - \sum^R(E)} \tag{3.9}$$

$$G^< = G^R \sum\nolimits^< G^{R^\dagger} \tag{3.10}$$

$$\sum^{<} = G^{<}D^{<} \tag{3.11}$$

$$\sum^{R} = G^{R}D^{R} + G^{R}D^{<} + G^{<}D^{R} \tag{3.12}$$

Where $\sum^{R}$ and $\sum^{<}$ are the retarder and lesser self-energies which describe various scattering mechanisms, and $D^{R}$ and $D^{<}$ are the sum of the retarded and lesser Green's function. The Eq. 3.9 and 3.10 are referred to as Dyson and Keldysh equations. Given an initial guess of the lesser Green's function, the self-energies are calculated in the self-consistent Born approximation. Then the retarded Green's function is calculated using the Dyson equation, and the lesser Green's function is calculated using the Keldysh equation. After convergence is reached, the current density and carrier density can be calculated directly from the Green's function as follows

$$\rho(E) = -\frac{i}{2\pi}\int dEG^{<}(E) \tag{3.13}$$

$$J_0(E,z) = \frac{e}{\pi S}\sum_{\alpha,\beta,\mathbf{k}} Re\left[\frac{-\hbar}{m(z)}\chi^{*}_{\alpha}(z)\frac{\partial\chi_{\beta}(z)}{\partial z}G^{<}_{\beta,\alpha,\mathbf{k}}(E)\right] \tag{3.14}$$

where $\chi_{\alpha,\mathbf{k}}$(z) is the envelope function in the growth direction $z$, and $S$ is the normalization factor. While the NEGF transport modeling is a powerful and accurate tool, it is computationally expensive, and therefore its use has been limited in the QCL community especially for the mid-infrared QCLs where there are many electronic levels, and axial energy ratios are much higher than the THz QCLs.

## 3.2 Two-material design

This design, referred to as the Forward Photonics device later in the chapter, was developed in our group for high efficiency operation and with the potential of scaling the power in a VECSEL configuration. It was grown in two different waveguide geometries, one with a thick cladding designed to minimize the waveguide loss for a ridge laser configuration, and another with thin cladding which was designed for our VECSEL project (refer to M.S. thesis of Eilam Morag for more details). The characterization data of both devices are presented

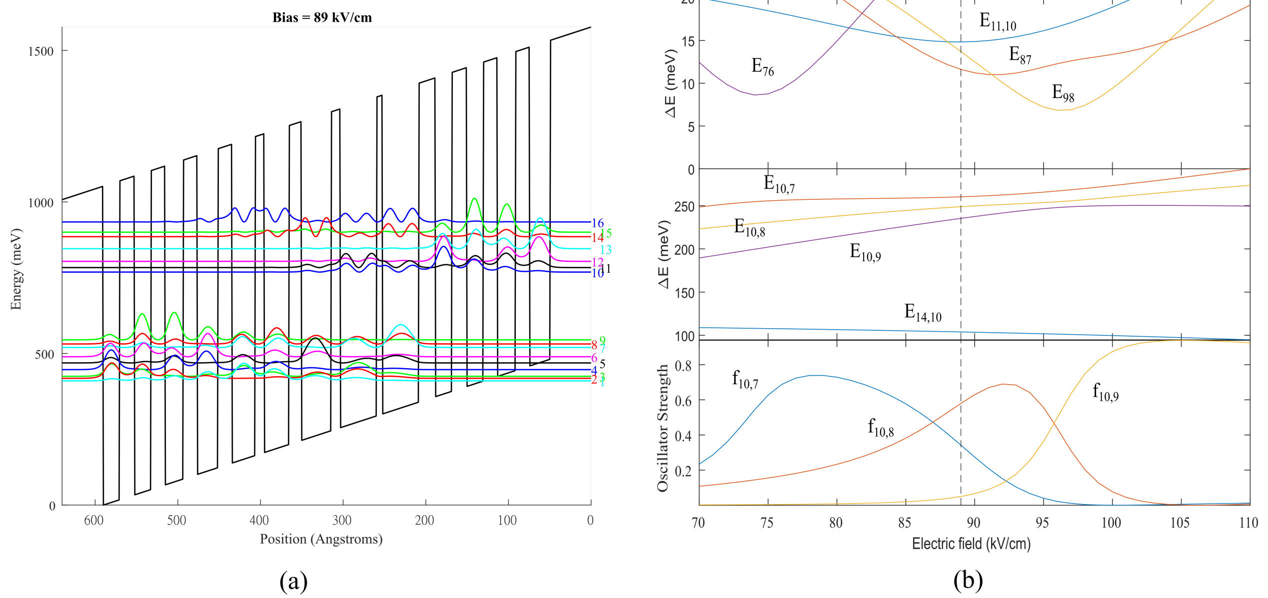


Figure 3.1: (a) Simulated bandstructure (electrostatic mean-field interactions are ignored) profile of FP 2-Material active region using shooting method Schrödinger solver. Well/barrier layers are strain-balanced $Al_{0.78}In_{0.22}As/In_{0.69}Ga_{0.31}As$, with average doping of $2.6\times10^{16}$ $cm^{-3}$ (b) Calculated anticrossing, energy separation, and oscillator strength versus electric field. The dotted line shows the design bias.

later in the chapter.

The active region is based on a three-quantum-well (3QW), with a larger first well that is designed to lase around 5 $\mu$m. This makes the transition less diagonal than the conventional 3QW design [57], which in turn increases the oscillator strength of the transition. The parasitic channel separation is increased by using tall barriers (conduction band offset is almost twice the lattice-matched case) and adjusting the well and barrier thicknesses in the active part of the module. The bandstructure at design bias, and the oscillator strength and anticrossing of key states are shown in Fig. 3.1.

The design bias is at 89 kV/cm, with injection anticrossing (coupling strength) of 15 meV and lasing transition energy and oscillator strength of 260 meV and 0.58, respectively. The large value of the oscillator strength is an indicator of a more vertical transition compared

to a diagonal one. The carriers are injected from the ground state $n = 11$ to the upper laser state $n = 10$, and radiative transition occurs from $n = 10$ to the lower laser states $n = 7$ and $n = 8$, with $f_{10,8}$ and $f_{10,7}$ of 0.58 and 0.34 respectively. The extractor states $n = 5$ and $n = 3$ are positioned below the lower laser level by 51 meV and 44 meV, respectively, and depopulate the lower level through LO phonon emission. These states are also in resonant with the injector states, which assists in efficient extraction of carriers from the lower states and an effective low lifetime for the lower lasing state.

## 3.3 Multi-material design

In this section, I describe the shallow-well design operating at 5 $\mu$m, which is the current state of the art efficiency in MWIR QCLs, and I will outline the steps I took to make a revised version of that with the hopes of increasing the efficiency. Additionally, I will present simulation results based on both rate equation model and self-consistent NEGF that was used to assess the improvement in efficiency.

The original design is based on the shallow-well design [2], as shown in Fig. 3.2b, which was designed for operation at 5 $\mu$m wavelength. It uses five different compositions for the wells and barriers to achieve high WPE through bandstructure engineering. Compared to the more conventional two-material design, the shallow-well design uses a close-to-lattice-matched well and barrier for the active region part of the module, in order to increase the parasitic channel separation from the upper laser level ($E_{11,10}$) and decrease the interface roughness scattering of the lasing transition. Additionally, it was shown that using the large AlAs barriers reduces the over-the-barrier leakage since the wavefunctions are more confined, and their coupling to the continuum states are reduced.

While this design has proved to be the state of the art so far in MWIR QCLs in terms of WPE, I investigate designs to further improve the WPE. Thus, a few steps were taken by bandstructure engineering, while trying to stay within the same composition of materials

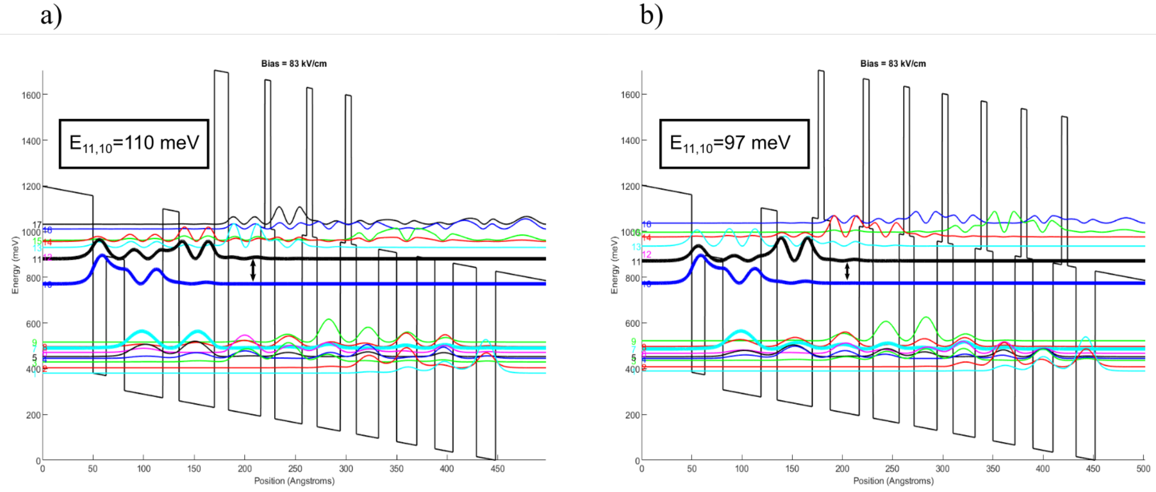


Figure 3.2: (a) Simulated bandstructure (electrostatic mean-field interactions are ignored) profile of the revised shallow-well design using shooting method Schrödinger solver and (b) the simulated bandstructure of the original shallow-well design [2].

used originally by Bai in Ref. [2]. The new design is shown in Fig. 3.2a. One of the main contributions to high WPE in the shallow-well design comes from the high parasitic energy separation from the upper laser level, $E_{11,10}$. One could try to increase this separation for even less leakage. Since the parasitic state is spatially confined on one end by the first tall barrier of the injector region, and the upper laser level probability density in that region is almost zero, increasing the barrier height can raise the parasitic level without changing the upper laser level energy. This was done by changing that barrier to be entirely of AlAs instead of AlAs/InAlAs. This increased $E_{11,10}$ by 13 meV compared to the original design, as shown in Fig. 3.2. The downside to this is a weaker injector coupling to the active region, which can be addressed by making the AlAs thinner to ensure proper coupling. It was found through the empirical rate equation simulations and also confirmed using NEGF modeling that a thickness of around 13 $\mathring{A}$ provides sufficient coupling while keeping the parasitic channel separated.

Next, to ensure the design is strain-balanced, the AlAs barriers from the last three

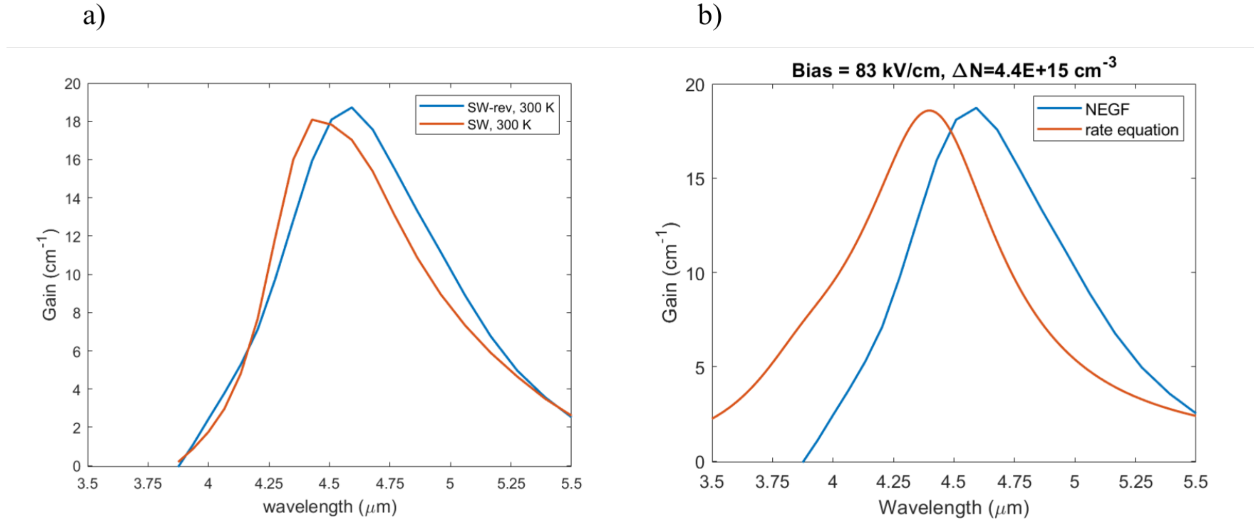


Figure 3.3: (a) Simulated gain using NEGF for the original shallow-well design compared to the revised design (b) Comparison of the simulated gain using rate equations and NEGF for the revised shallow-well design.

injector barriers were removed. The main purpose of using tall barriers is to minimize over the barrier leakage, and the last three barriers seem to play a minor role for that purpose. Other adjustments were also done such as reducing the width of the last two injector wells to reduce the voltage defect and localizing the ground state in the last well to avoid parasitic injection.

### 3.3.1 Rate equations versus NEGF calculation

In this section, I compare the results from the empirical rate equation model to the ones from the more sophisticated NEGF modeling. Specifically, the gain spectra is calculated using both methods, and key differences are discussed. First, obtaining the gain spectra using the rate equation model requires knowledge of parameters such as the oscillator strengths, transition linewidth, effective mass, dielectric constant, and population inversion. The population inversion can be found iteratively using the empirical rate equations. Here I estimate a value of $4.4\times10^{15}$ cm$^{-3}$ given an average doping density of $2\times10^{16}$ cm$^{-3}$. This value was found by

matching the gain spectra to the one from NEGF simulations. Next, the linewidth of the transition can be found using the lifetime of the upper and lower state, which is calculated to be 1.22 ps and 0.063 ps, respectively. Ignoring the pure dephasing term ($T_2^*$), a linewidth of 0.175 $\mu$m is calculated from Eq. 2.24. However, using a phenomenological dephasing value of $T_2^*$=42 fs will increase the linewidth to 0.76 $\mu$m, which will match the gain spectra from the NEGF simulation, as shown in Fig. 3.3b. This shows the important effect of the pure dephasing on the linewidth, which cannot be ignored. The shift in the peak frequency of the gain is due to the slightly different values for the conduction band offsets in the material database, which cause slight shift in the levels and thus the lasing transition frequency.

Also, it is worth noting that including the temperature dependence in the rate equations is not as straightforward and accurate, since it is accounted for using a thermally activated model for thermal backfilling from the ground reservoir into the lower level, and also from the upper level into the parasitic states. However, the NEGF solver has the capability of accounting for these effects as well as the broadening of the levels in energy due to increased scattering. This is a clear advantage of using NEGF solver for evaluating efficiency, as the temperature performance is a key metric for high efficiency continuous wave operation.

### 3.3.2 Compare to original design

Based on the empirical rate equation model, an slight increase in the WPE is expected compared to the original design. To check this, the nextnano software is used to simulate the power density and internal WPE. To do so, the photon-assisted transport feature is used, which defines an EM mode at a given frequency, and finds the mode intensity self-consistently as the modal gain reaches the cavity loss, where the modal gain is defined by gain times the confinement factor. Here, an EM mode is defined at 270 meV (4.6 $\mu$m), and a cavity loss of 2.76 cm$^{-1}$, and a confinement factor of one is assumed. Starting from zero intensity, the EM field is adjusted self-consistently until the lasing threshold is met ($g_c$=$\alpha$). The photon-assisted transport is evident in the current-voltage plot shown in Fig. 3.4a,

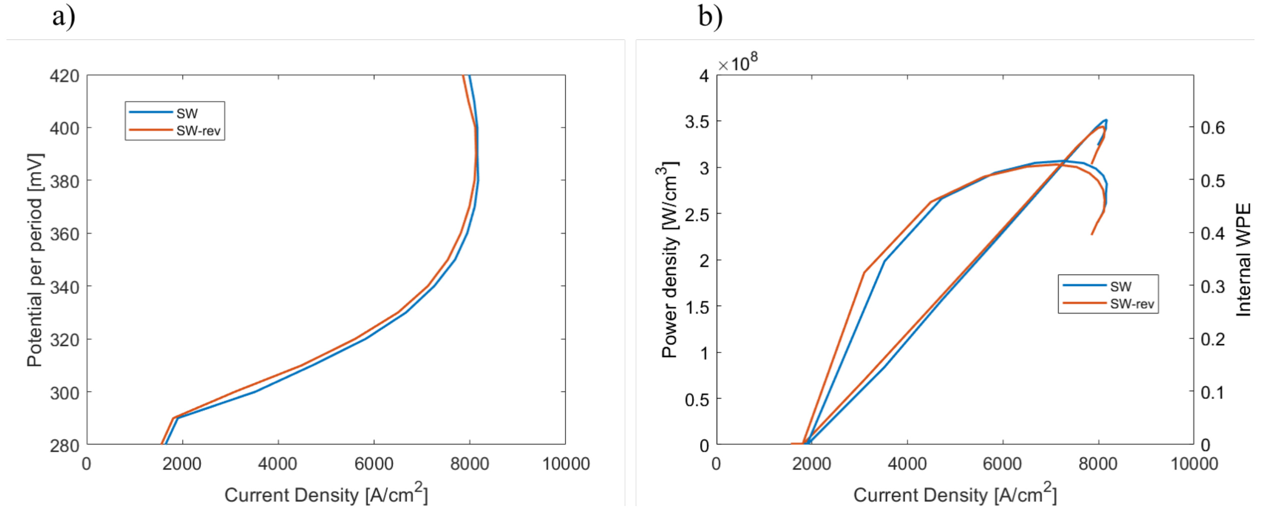


Figure 3.4: Simulated (a) current-voltage characteristics of the original and revised shallow well design and (b) WPE and power density calculated using NEGF solver in nextnano package. Photon-assisted transport is enabled for an EM mode at 270 meV.

where there is a sudden increase in current at the onset of lasing. The calculated power density and internal WPE is shown in Fig. 3.4b, where the internal WPE is defined as the ratio of the optical output power to the electrical input power

$$\eta_{\text{WPE}}^{\text{internal}} = \frac{P_{\text{stimulated emission}} - P_{\text{absorption}}}{UI} \tag{3.15}$$

and the losses due to the mirror and cavity are ignored. The external WPE is then calculated using the mirror and cavity losses as follows

$$\eta_{\text{WPE}}^{\text{external}} = \eta_{\text{WPE}}^{\text{internal}} \frac{\alpha_{\text{fm}}}{\alpha_{\text{cavity}}} \tag{3.16}$$

Although the revised design was initially expected to exhibit a higher WPE due to the increased energy separation of the parasitic channel, the nextnano simulations suggest that there is no improvement in efficiency. This is also supported by the fact that their simulated gain spectra have almost the same peak value, as shown in Fig. 3.3a. Therefore, perhaps the effect of leakage to parasitic channel is not as severe as it was thought to be originally, and other methods should be tried to increase the efficiency, such as optimizing the voltage defect and effective lifetime of the laser.

Therefore, although rate equations remain a powerful tool due to their simplicity and computationally efficient nature, this result suggests that they should perhaps be complemented with a more accurate self-consistent NEGF modeling for optimizing the design efficiency.

## 3.4 Fabrication development

### 3.4.1 Process flow

In this section, I outline the fabrication process flow that I developed for making ridge lasers from our MWIR QCLs. The process flow is shown in Fig. 3.5, and is listed in detail in Appendix A. The mask contains ridges of different widths and circular mesa structures for electroluminescence measurement. The etch chosen for this process is a wet etch based on HBr. The is because the top contact is evaporated after the ridges are etched, and a vertical sidewall would make it difficult to achieve conformal metal coverage. After the process is completed, the devices can be mount either epi-up or epi-down, although the devices fabricated in this work were mounted epi-up since improving heat extraction was not emphasized. A top down view of the fabricated device is shown in Fig. 3.5, where the yellow is the top gold contact, and the purple area is the oxide area for electrical insulation. The process starts with oxide mask deposition using the STS-PECVD tool (1HFO recipe). The oxide is then patterned and BOE etched, and the oxide ridges are used as the etch mask for the wet etch process.

Next, the piece is etched into ridges using the etch solution HBr:HCl:$H_2O_2$:$H_2O$ (10:5:1:50) [42]. The solution is prepared as follows. First, one needs to pay attention to the poisonous nature of HBr and take safety precautions by reading the corresponding MSDS of the chemical. When mixing the solution, $H_2O_2$ should be added last, and acid should be added to water, not the other way around. After mixing the correct ratios, a 20 minutes wait time is needed to ensure sufficient oxidization of the solutions. During this wait time, the solution color changes from a pale orange to an intensely dark red color, and this is normal. The etch

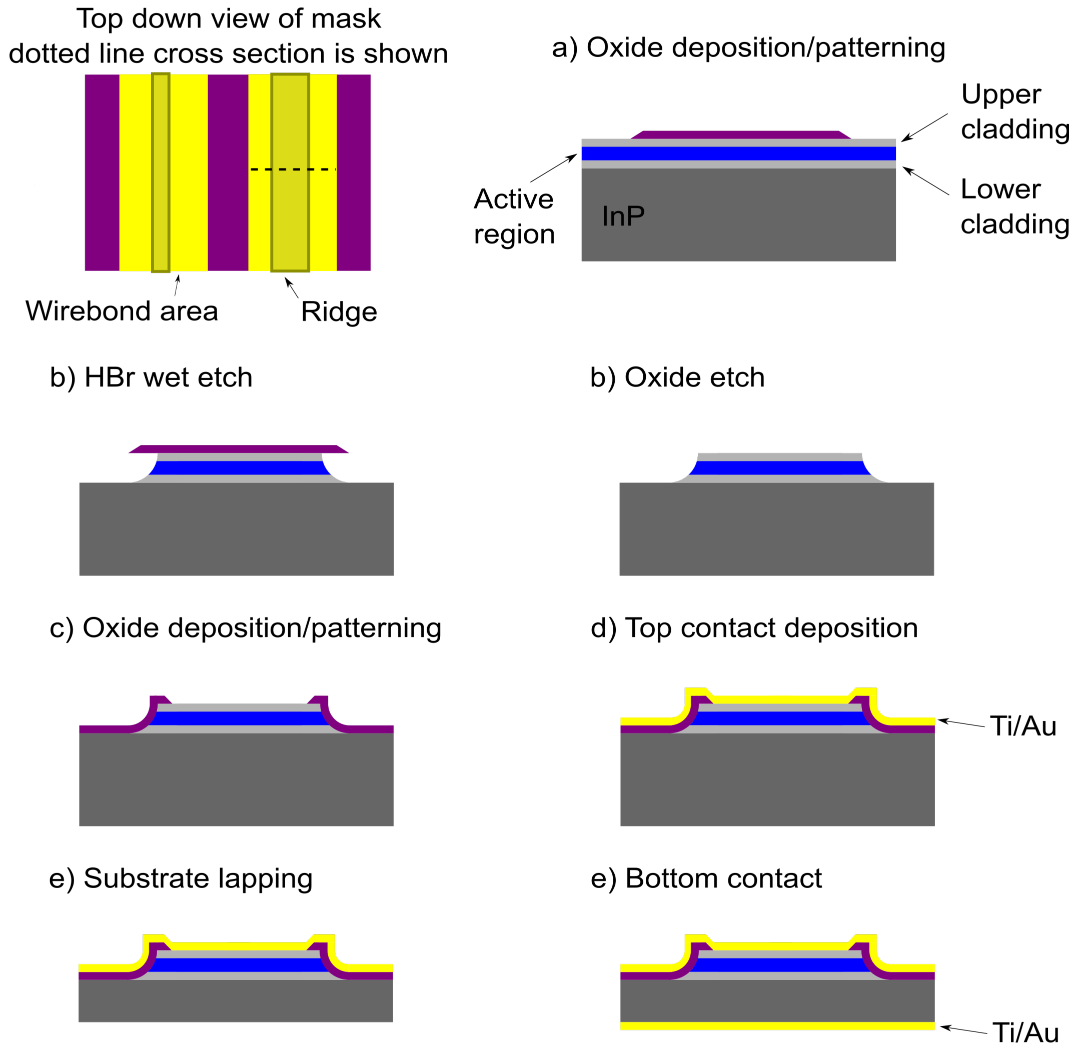


Figure 3.5: MWIR QCL ridge fabrication process flow.

depth is measured every minute to get the etch rate, and the process is continued until the desired etch depth is achieved. The etch rate was around 1 $\mu$m/min and slowly decreased as the etchants were used up. The vertical/lateral etch ratio is around 1.2 to 1.8, although these depend on the specific active region and growth.

After the ridge etch process is completed, the oxide mask is removed using BOE solution, and the ridges are inspected under the microscope to measure ridge widths and ensure uniformity. Then, a layer of insulating oxide (around 250 nm) is deposited using the STS-

PECVD tool. This oxide layer is then patterned and BOE etched to make the top opening for the contact. Note that wet etch is preferred over dry etch for making the top opening due to its isotropic nature which provides a smooth transition for top metal contact, as shown in Fig. 3.5c.

The Ti/Au top contact is then evaporated using the Sloan evaporator tool. Due to the top of the ridge exhibiting a nearly vertical slope, this evaporation is done at an angle of around 15 degrees. This tilting of the sample causes shadowing of the metal, therefore care must be taken to orient the piece such that the wirebond area side is facing down and is coated.

The substrate was then lapped down to 150 $\mu$m using the PM5 polisher tool. This step is encouraged if the substrate is thicker than 350 $\mu$m to begin with, since it would make cleaving small ridge length difficult if not impossible in practice.

Finally, the Ti/Au back contact is evaporated using the Sloan evaporator tool.

### 3.4.2 Challenges and solutions

There has been a few challenges in developing the process flow, especially for the wet etch process. The mid-IR QCL growth stack consists of multiple layers grown on the InP substrate: Lower cladding (InP), bottom InGaAs layer, active region (InGaAs/InAlAs), upper InGaAs layer, top cladding (InP), and highly doped InGaAs contact layer. Therefore, a desired wet etch recipe needs to have the following qualities: isotropic (independent of crystallographic direction) and non-selective (equal etch rate between different materials (InP, InGaAs, InAlAs)). The first challenge was to find the suitable wet etch recipe that has the aforementioned properties.

The first attempt was using 3 separate solutions to etch the ridges: 1) $H_2SO_4$:$H_2O_2$:$H_2O$ (1:1:10) to etch the top InGaAs contact layer, 2) HCl:$CH_3COOH$ (1:3) to etch the top InP cladding layer, 3) HBr:$HNO_3$:$H_2O$ (1:1:10) to etch the active region [12]. The etch profile is

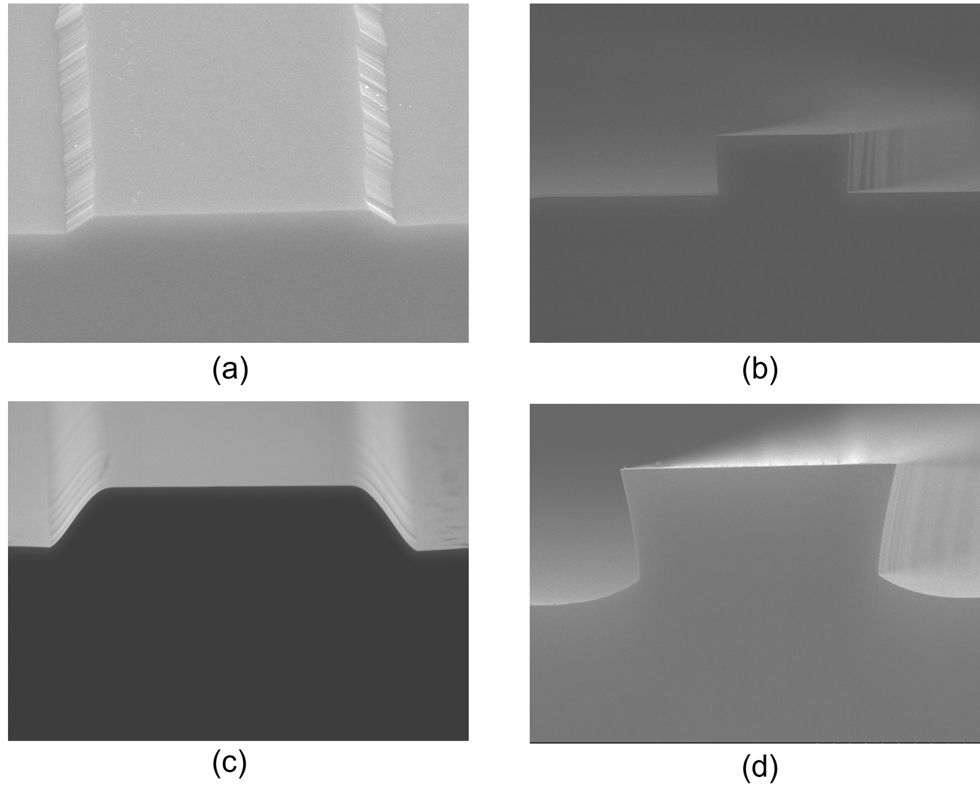


Figure 3.6: HCl:$CH_3COOH$ etch profile for ridge oriented (a) perpendicular and (b) parallel to the wafer major flat. HBr:$HNO_3$:$H_2O$ etch profile for ridge oriented (c) perpendicular and (d) parallel to the wafer major flat. Result provided by Dr. Sudeep Khanal.

shown in Fig. 3.6 for different ridge orientations. This etch had several drawbacks. First, the etch profile depends on the ridge orientation with respect to the wafer flat. In other words, they are not isotropic. This makes the processing difficult since one needs to keep track of the wafer orientation. Second, the solution in the last etch (HBr:$HNO_3$:$H_2O$) needs to rest for 24 hours before starting the etch. And since HBr is light sensitive, proper measures need to be taken to minimize light exposure during the resting time. And third, the etch is cumbersome due to having multiple steps. The advantage of this etch recipe is the sloped sidewall at the top of the ridge, which allows for vertical top contact deposition instead of tilted deposition.

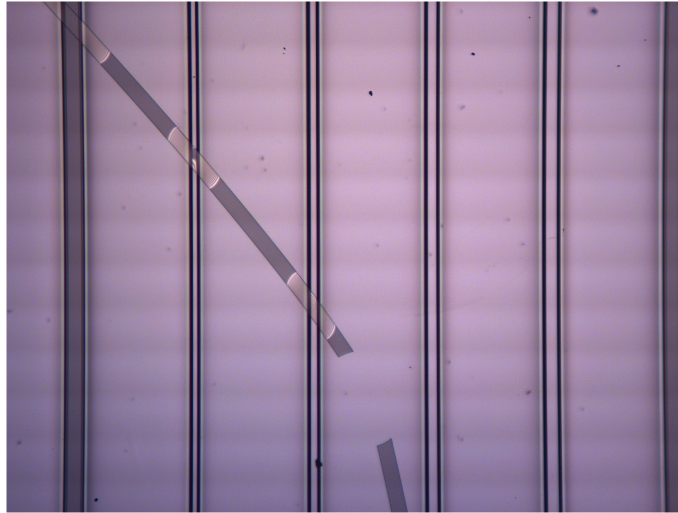

Figure 3.7: Photoresist delamination after HBr wet etch.

Following the aforementioned discussion, author decided to use an alternative etch, initially discussed in Ref. [42], and also currently used in many mid-IR ridge fabrication processes. The etch solution is HBr:HCl:$H_2O_2$:$H_2O$ (10:5:1:50). This etch has several advantages: It is isotropic, non-selective, one-step, and not intensively time consuming.

The next challenge was associated with the etch mask used for the wet etch process. Photoresist is a common etch mask for wet and dry etches. It provides the advantage of reducing the number of fabrication steps compared to an oxide or nitride mask. Thus, a photoresist mask (AZ5214E) was initially used as the etch mask. However, the photoresist mask delaminated during the wet etch, as shown in Fig. 3.7. The reason for the delamination is unclear, but suspected to be related to the poor adhesion of the resist and the swirling of the piece during the etch. Therefore, to resolve this issue, an oxide mask was used instead.

Finally, the nearly-vertical sidewall at the top of the ridge caused a complication for top contact deposition. Fig. 3.8a shows the case when top contact was done vertically, and it can be seen that the metal coverage is not conformal. This caused an open during the IV characterization, most likely due to the very thin contact burning at the top. This was resolved by doing a tilted evaporation instead, as shown in Fig. 3.8b.

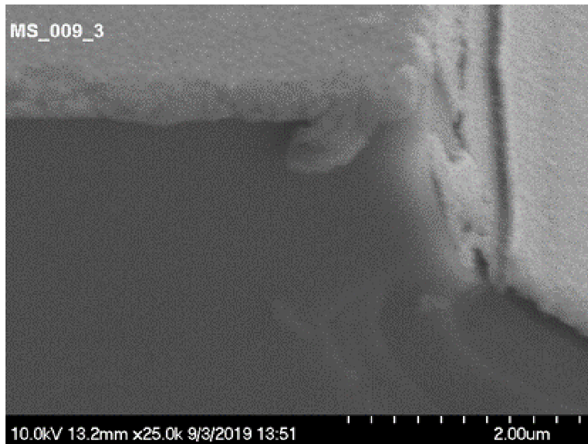


(a)

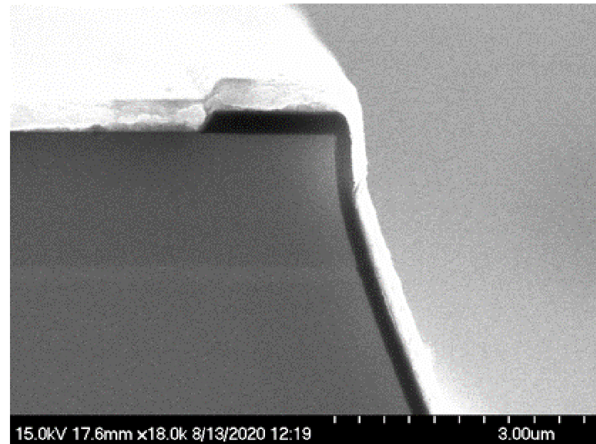


(b)

Figure 3.8: Top contact evaporated (a) vertically and (b) at an angle.

## 3.5 Characterization

After the fabrication of the device is complete, it is characterized using standard QCL characterization techniques. This reveals valuable information about the device such as existence of parasitic channels, average sheet doping density, threshold current density, and negative differential resistance (NDR).

To do so, the fabricated piece is cleaved into ridge bars of a few millimeters length. The piece is then mounted epi-side up on a copper mount using indium foil and flux. The application of flux onto the copper mount and indium foil removes the oxidized layer and enhances the bond quality. The device is then wirebonded onto a gold pad, that is also mounted onto the copper mount using a higher melting temperature solder that contains silver. The device is then inserted into a dewar if cryogenic operating temperatures is required, or mounted on a thermoelectric cooler for temperature dependent measurements above and below room temperature.

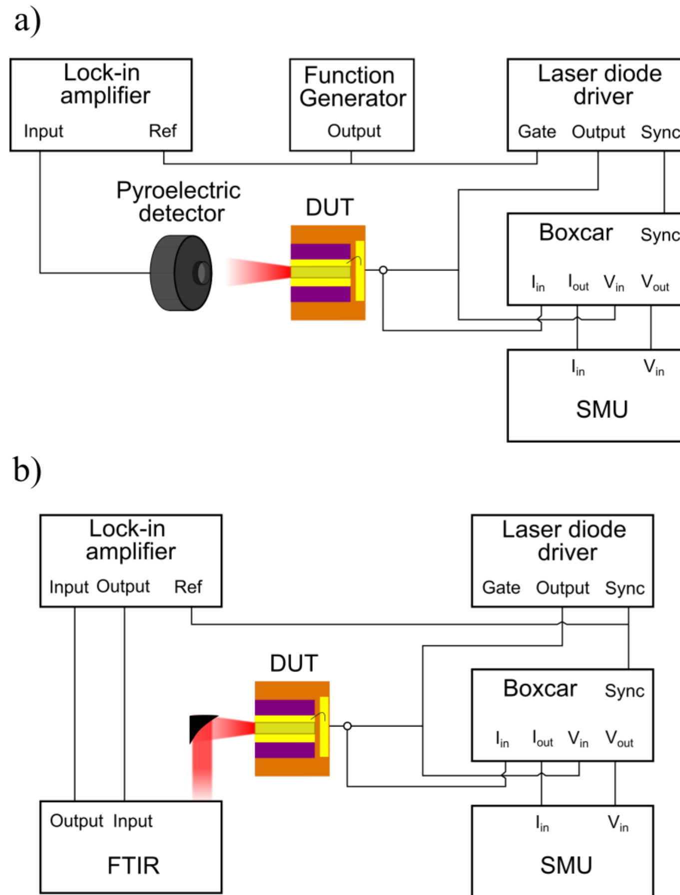


Figure 3.9: Characterization setup for (a) light-current-voltage measurement and (b) electroluminescence measurement.

### 3.5.1 Equipment and setup

The characterization setup for measuring L-I-V and electroluminescence are shown in Fig. 3.9. To bias the laser at low duty cycle and small pulse widths, a laser diode driver (Avtech pulser) is used which can provide pulse widths as small as 100 ns. The pulse train from the laser driver is gated at a low frequency (40 Hz) using a square pulse, which means the laser is on for 12.5 seconds and off for the same amount of time in every period. This gating is done since the pyroelectric detector is sensitive to changes in optical power (produced heat), and therefore it is not suitable for detecting continuous wave signals. The voltage across

the device is measured using an SMA Tee-adapter, and the current going into the device is measured using a current sensor that has an inductive loop. These signals are input into a boxcar, the gate of which is shorter than than the pulser output, and is centered on the pulse by adjusting the delay of the pulser. Additionally, the laser diode driver and boxcar are synchronized together. The boxcar averaged output is then measured using a source meter unit (SMU) for both current and voltage. Lastly, the output of the pyroelectric detector is input into a lock-in amplifier, which is referenced at the function generator's gate signal.

The electroluminescence is measured using step scan feature of the FTIR (Nicolet), as shown in Fig. 3.9b. The signal is detected using a cooled MCT detector, and a KBr beamsplitter. The detector output of the FTIR is connected to the lock-in amplifier, and the output of the lock-in is sent back to the input of the FTIR, and the sync signal from the pulser is connected to the reference of the lock-in amplifier. Since spontaneous emission signal is very weak, a good alignment is essential. This is done by running the QCL in lasing mode and maximizing the peak to peak signal on the interferogram of the FTIR. Then the pulser voltage is set to subthreshold values, and the FTIR is run in step scan mode. To increase the signal to noise ratio, one can increase the settling time, average time per step, and the number of scans. However, as long as the delay time is a few times the integration time constant of the lock-in amplifier, the blackbody background is eliminated. Typically, a reasonable signal to noise ratio was achieved in a 20 minutes scan with a resolution of 32 $cm^{-1}$.

### 3.5.2 Forward Photonics device

The device described in this section was grown by IQE (Substrate PN: 223F3-BNL48-00) and processed by Forward Photonics. The active region is based on a strain-compensated $Al_{0.78}In_{0.22}As/In_{0.69}Ga_{0.31}As$ with average doping of $2.6 \times 10^{16}$ $cm^{-3}$. The fabricated wafer was mounted epi-side up, and a 10 $\mu$m $\times$ 3.5 mm ridge was characterized. Fig. 3.10a-b shows the LIV and WPE characteristics of the device in pulsed mode (10 kHz repetition

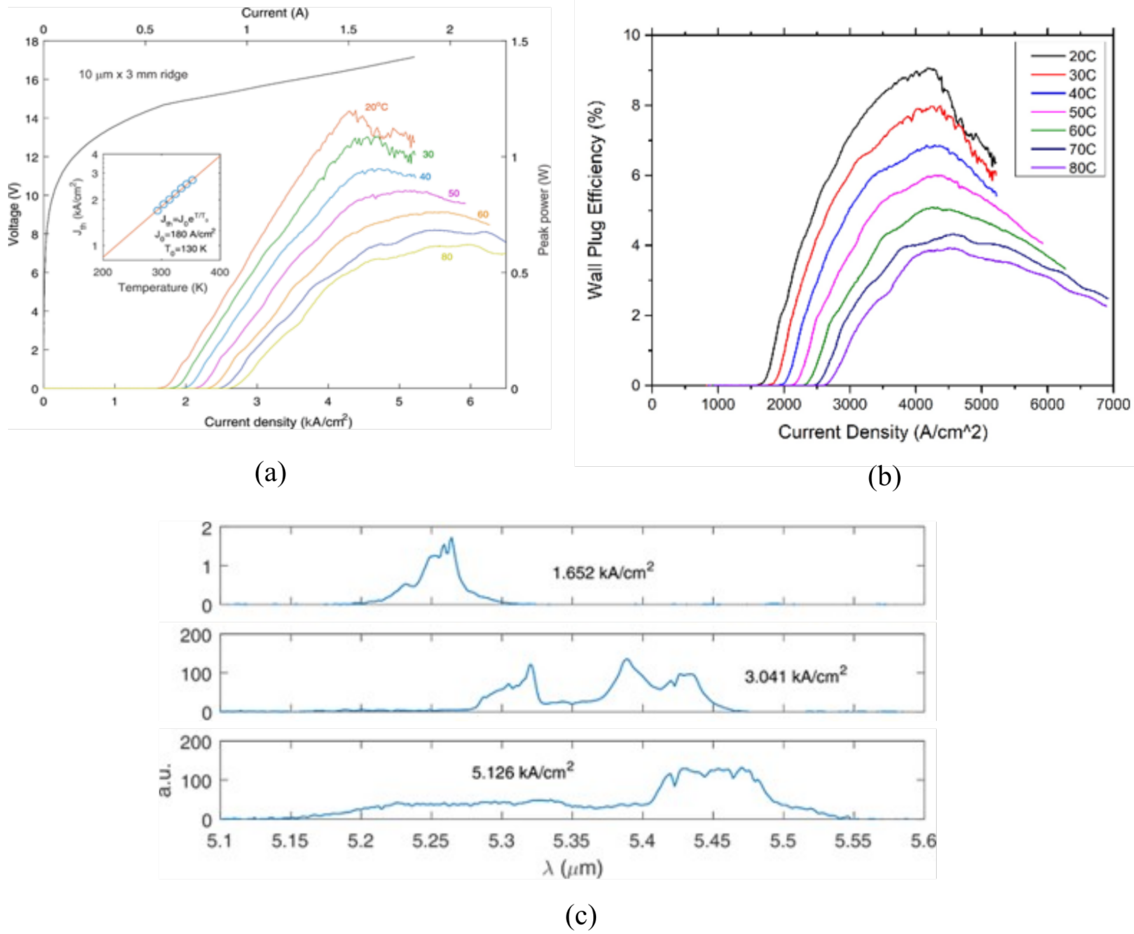


Figure 3.10: (a) 223F3-BNL48-00 temperature dependent L-I-V and (b) wall plug efficiency. (c) Spectra at room temperature and 1% duty cycle.

rate, 1 $\mu$m pulse width). A threshold current density of 1.7 kA/cm$^2$ and a slope efficiency of 1.29 W/A was measured at room temperature, with characteristic temperatures of $T_0$ = 130 K and $T_1$=156.7 K. The power was measured from one facet (uncoated) using a calibrated thermopile detector, with maximum peak power of 1.12 W and wall plug efficiency of 9.1%. The spectra of the device is shown in Fig. 3.10c. The lasing spectrum varied from 5.2 $\mu$m to 5.5 $\mu$m over the dynamic range of the device, exhibiting a red shift with increasing bias.

Compared to the similar two-material system by Lyakh et.al [34], the device exhibited similar $J_{th}$ and $T_0$, however the total power, dynamic range, and slope efficiency were lower.

This suggests higher loss for the device, since InP regrowth was not done, and metal cladding is much more lossy than InP cladding. Nevertheless, the device seemed to be a good candidate for our mid-IR VECSEL design.

### 3.5.3 Forward Photonics device - thin cladding

This device is a modification of the previous device, but with a thinner upper cladding layer to work in a VECSEL configuration. It was grown by IQE (Substrate PN: 22851-BNL48-01) and fabricated/ characterized by the author at UCLA.

For comparison, two ridge widths (8 and 25 $\mu$m) of the same length (3 mm) are tested. Characterization is done in pulsed mode (10 kHz repetition rate and 500 ns pulse width, 0.5 % duty cycle) and for temperatures from 78 K - 250 K. From the temperature dependence of $J_{th}$ and $\eta$, characteristic temperatures of $T_0$ = 232 and $T_1$ =129 for the 8 $\mu$m ridge, and $T_0$ = 198 and $T_1$ =127.5 for the 25 $\mu$m ridge are extracted. Power was measured from one facet without HR coating. Peak power is calculated for one facet while also accounting for 70% transmission of the ZnSe window of the cryostat.

The LIV and cross section SEM of the 8 $\mu$m ridge is shown in Fig. 3.11a-b. Compared to the previous design with a thicker upper cladding, this device exhibited much lower total power and efficiency. This is partly explained by the additional loss coming from the mode interaction with the top contact, since in general a smaller upper cladding results in higher waveguide loss. This is also evident from the increased threshold current density (3.25 kA/cm$^2$ versus 1.7 kA/cm$^2$). The other reason is probably due to the substrate being low doped (2-5$\times10^{16}$ cm$^{-3}$), which was done purposefully to minimize the VECSEL loss, but this reduces the InP mobility and conductivity, and makes the Ti/Au back contact Schottky instead of ohmic contact [39]. This is seen from the high voltage drop in the IV plot.

The 25 $\mu$m and 6.5 $\mu$m wide ridges lased up to 200 K and 260 K, with maximum wall plug efficiency of 0.2% and 0.73%, and minimum threshold current density of 4.71 kA/cm$^2$ and

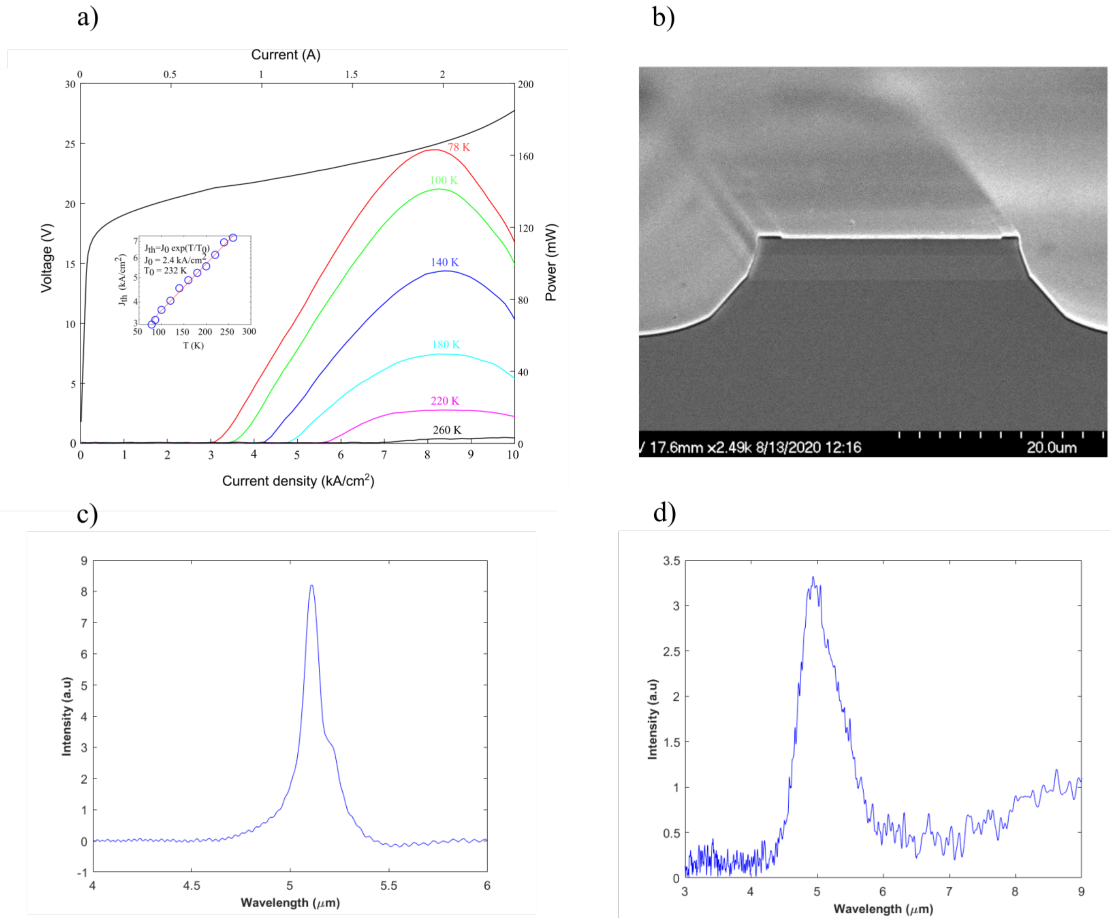


Figure 3.11: (a) 22851-BNL48-01 temperature dependent L-I-V for the 8 $\mu$m ridge. (b) Cross section SEM of the fabricated 25 $\mu$m ridge. (c) Spectra at 77 K and (d) electroluminescence at 300 K.

3.25 kA/cm$^2$ at 78 K respectively. From the electroluminescence and lasing spectra, shown in Fig. 3.11c-d, the emission frequency shifts from 4.9 $\mu$m to 5.2 $\mu$m as the temperature is varied from 300 K to 77 K.

# CHAPTER 4

# VLWIR QCL: design, fabrication, characterization

## 4.1 Introduction

In this chapter, I will discuss the design of our very-long-wavelength-IR (VLWIR) QCL designed to operate at 20 $\mu$m, along with the development of the fabrication process and the characterization methods. This project is an effort to extend our metal-metal waveguide configuration to the far-IR frequencies, with the possibility of making high power, single mode tunable VECSELs.

The wavelength range of 16 - 25 $\mu$m, referred to as the VLWIR, is of special interest due to the atmospheric transmission window in that region. Additionally, it lies close to the far-IR region from 20 - 60 $\mu$m, which is also of great interest for various applications such as identifying aromatic hydrocarbons in astrochemistry and studying the cosmic microwave background radiation (CMBR) [15]. However, unlike its neighbouring mid-IR and THz regime, the far-IR still remains underdeveloped due to most optical materials and semiconductors exhibiting strong dispersion and absorption in the region due to the *Reststrahlen* band of those materials, which lies between their longitudinal optical (LO) and transverse optical (TO) phonon frequencies. This band for typical III-V material is around $\lambda$ = 20 - 60 $\mu$m. QCLs are currently one of the leading sources that are bridging the gap between mid-IR and THz, while more development is still needed in the detectors and materials to bring far-IR back to the fold.

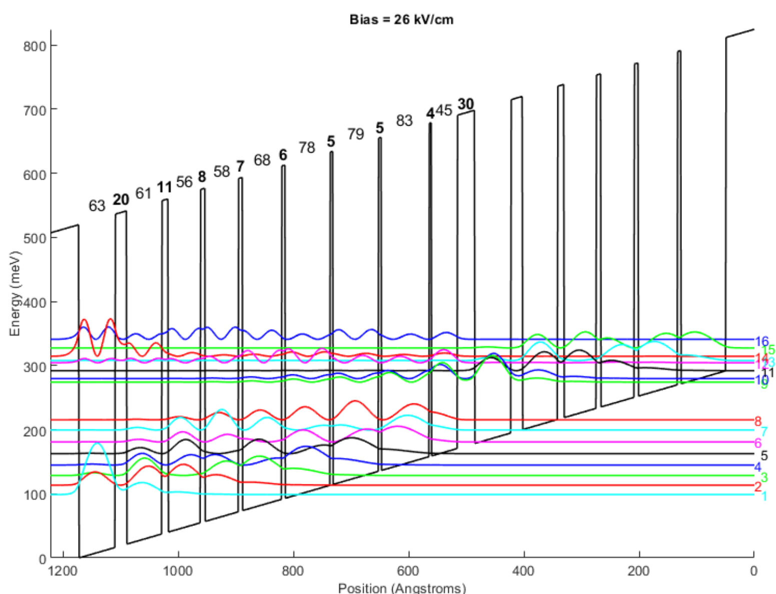


Figure 4.1: Bandstructure of the 20 $\mu$m QCL.

## 4.2 Active region design

I based my active region design on a previously published bound-to-continuum design at 24 $\mu$m [37]. Due to the lasing transition being close to the phonon modes of the material where there is high absorption, reasonable upper level lifetimes are difficult to achieve. Additionally, the active region needs to be thick enough to avoid the losses coming from the InP cladding and substrate. To address the aforementioned concerns, the laser transition from 9→8 is made diagonal to increase the upper level lifetime at the cost of a smaller oscillator strength, and the waveguide is chosen to be a metal-metal (MM) waveguide, which increases the mode confinement and decreases the losses coming from the semiconductor waveguide. To design the active region to operate at 20 $\mu$m instead, several steps were taken. First, the module length was increased by approximately 4 nm to keep the design bias around 24 kV/cm. This was accomplished by adding an extra pair of well and barrier to the injector region. Next, the first well in the active region was decreased by 9 $\AA$ to increase the upper and lower level

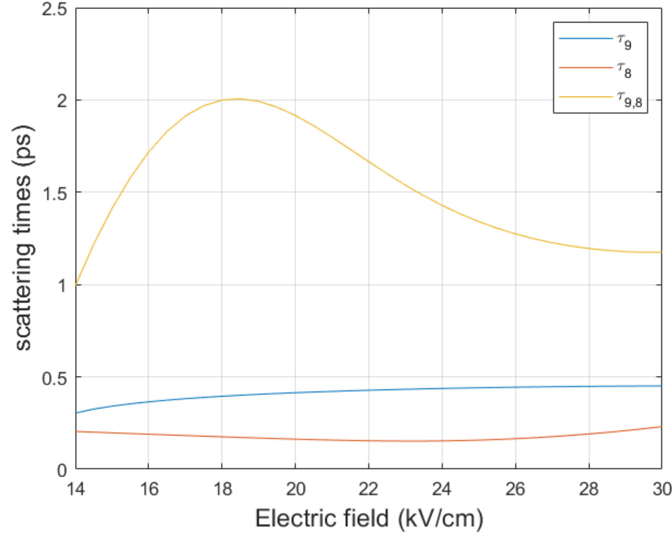


Figure 4.2: LO phonon scattering times versus bias for lattice temperature of 300 K.

separation to 62 meV. Also, in an effort to avoid leakage to the higher parasitic states, all the well widths were decreased by a few Angstroms. This works since the higher parasitic states are excited states, and their energy increases more rapidly as the well width is decreased. The bandstructure of the final design is shown in Fig. 4.1. Layer sequence of one period is as follows: **30**/45/**4**/83/**5**/79/**5**/78/**6**/68/**7**/58/**8**/56/**11**/<u>61</u>/**20**/63 [$\mathring{A}$], where $In_{0.52}Al_{0.48}As$ barriers are in bold, $In_{0.53}Ga_{0.47}As$ wells are in normal font, and the underlined layer is doped at $4.25\times10^{17}$ cm$^{-3}$. The dipole matrix element of the transition from 9→8 is 5.52 nm, and the normalized oscillator strength is 2.12, making this a diagonal transition with an upper and lower state LO phonon scattering lifetime of 0.44 ps and 0.17 ps, respectively. Fig. 4.2 shows the bias dependent LO lifetime of states 9, 8, and 9-8 which is relevant for gain calculations. Assuming that the lifetime is limited by the LO phonon lifetime, it is deduced from the lifetimes that there is population inversion over a large range of biases, which means that a high dynamic range can be expected from this design. This makes sense since there is no resonant condition for the bound-to-continuum design as there is for other popular designs such as the double-phonon resonance design.

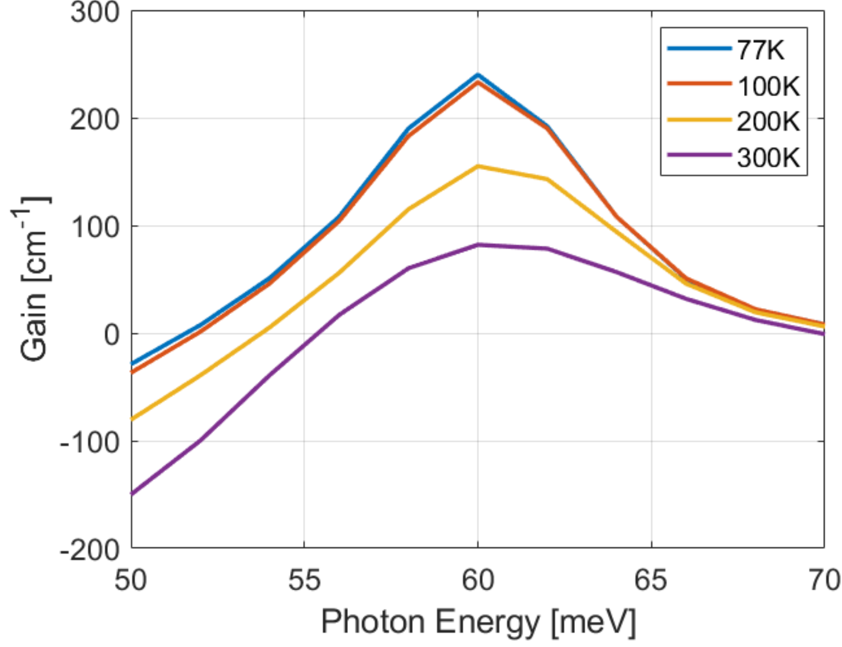


Figure 4.3: NEGF simulation of gain versus lattice temperature for 20 $\mu$m QCL.

The scattering from interface roughness and alloy disorder are ignored in this lifetime calculation. These lifetime values suggest there is probably gain available at room temperature, and lasing might be possible. However, the waveguide losses are substantial at 20 $\mu$m, since it is close to the absorption from the phonon modes of the material. This will degrade the device performance and will likely prohibit lasing altogether. Additionally, the effective electron temperature is much higher than 300 K, which means the leakage to the parasitic channels and also over the barrier can be significant.

To explore this further, transport modelling based on NEGF is performed using nextnano simulation tool, which provided the gain spectra and current density. Fig. 4.3 gives the simulated gain spectra versus temperature. There seems to be in excess of 80 cm$^{-1}$ of gain at room temperature, which is already higher than the calculated waveguide loss of around 53 cm$^{-1}$ for the 24 $\mu$m design [37]. Given that the 20 $\mu$m is further away from the AlAs phonon mode, an even smaller waveguide loss is expected which will likely facilitate lasing

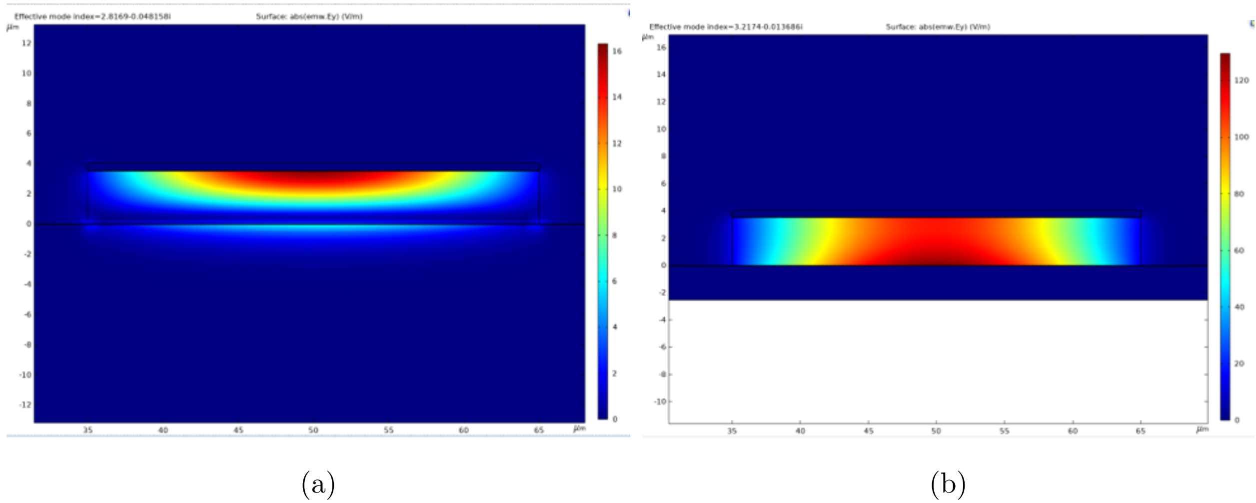


(a) (b)

Figure 4.4: (a) Surface plasmon and (b) MM waveguide mode profile.

of this new design at room temperature. To explore this further, it is important to consider the waveguide, and the effect of high doped layers on the losses.

## 4.3 Waveguide design

In the surface plasmon waveguides initially used for VLWIR QCLs, the mode is usually confined to the active region by using high doped InGaAs layers which behaves like a metal and provides refractive index contract. However, this method still gives subpar confinement factor and high losses coming from the high doped InGaAs layers and the mode penetration into InP substrate [47]. This results in substantial increase in threshold current densities and low operating temperatures. A solution to this is to use a MM waveguide, which provides close to unity confinement factor and lower waveguide losses compared to the surface plasmon waveguide. To show this, a finite element method electromagnetic simulation is performed using COMSOL Multiphysics software, which gives the mode index of the fundamental mode. The loss is accounted for by finding the conductivity of each layer and including that in the permittivity of the material using the Drude model. The waveguide loss is then calculated

from the imaginary part of the mode index, using the following formula

$$\alpha_w = \frac{2n^{''}\omega}{c} \tag{4.1}$$

where $n^{''}$ is the imaginary part of the mode index, $\omega$ is the angular frequency, and $c$ is the speed of light.

The simulated mode profile for the surface plasmon and MM waveguide is shown in Fig. 4.4. It is evident that the confinement factor for the surface plasmon case is much smaller than the MM waveguide design. The loss is also decreased from 171 $cm^{-1}$ to 88.5 $cm^{-1}$, due to the mode not being confined in the high doped lossy substrate. To further reduce the loss for the MM waveguide case, the highly doped top InGaAs contact layer can also be etched. This reduces the loss down to 34 $cm^{-1}$ at the cost of increased voltage drop from the Schottky contact and reduced efficiency. The waveguide loss was shown to be almost independent of the ridge width down to 10 $\mu$m, below which the mode starts to leak outside of ridge and interact more heavily with the top gold contact.

The Lattice matched design was grown on InP substrate by MBE at IntelliEPI, Inc. After growth of 40 nm highly doped n-$In_{0.53}Ga_{0.47}As$ bottom contact layer, 50 repetitions of the module was grown and capped with 40 nm of highly doped n-$In_{0.53}Ga_{0.47}As$ top contact layer. The total growth thickness was around 3.5 $\mu$m. In the next section, I will discuss the fabrication process flow developed to make the MM waveguides.

## 4.4 Fabrication

The fabrication process flow is shown is Fig. 4.5. The mask contains ridges of different sizes (50, 20, and 15 $\mu$m). For the small ridges, it is difficult if not impossible to wirebond directly on top of the ridge, thus a bias pad is inserted next to those ridges, which are connected to the actual ridge using small bridges (not suspended). Additionally, the bias pads are insulated with oxide to avoid unintentional biasing and current spreading.

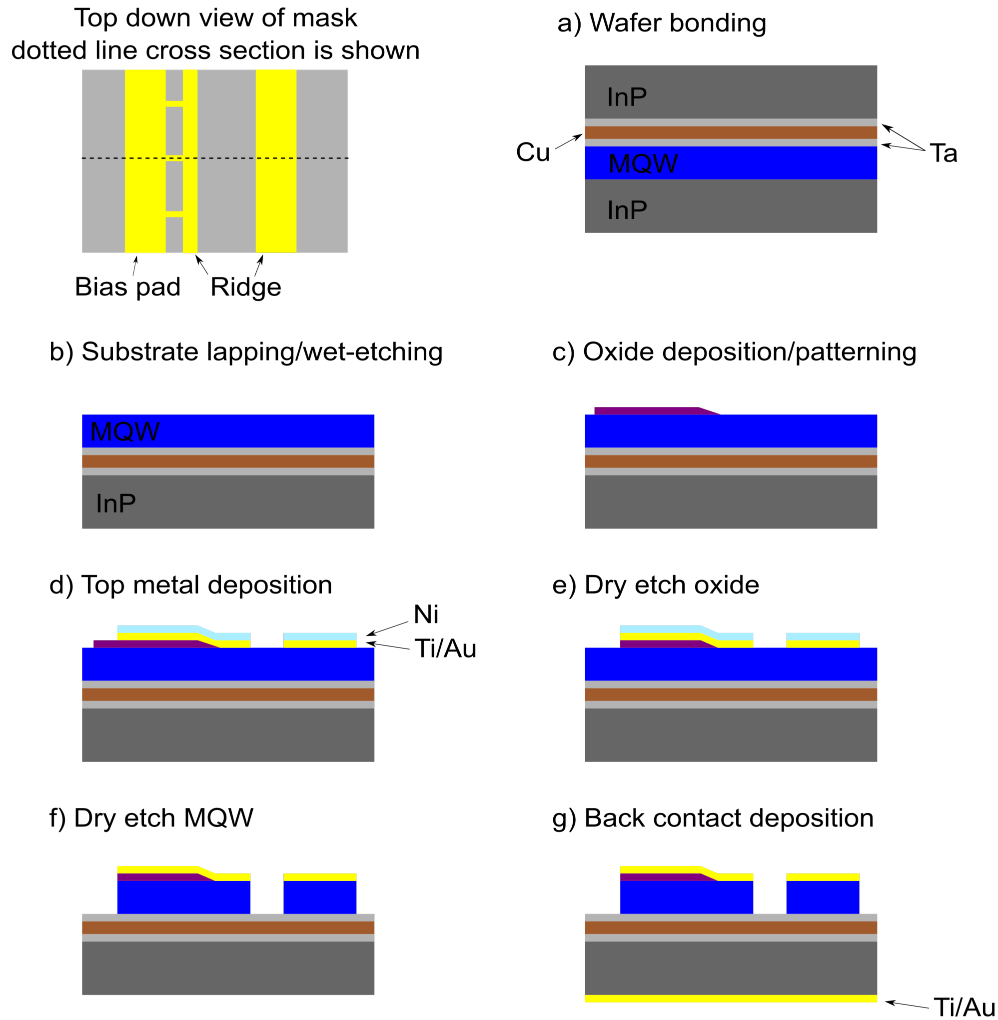


Figure 4.5: Fabrication process flow for 20 $\mu$m QCL.

Initially, a tantalum/copper (Ta/Cu) layer is deposited on the sample and on the InP receptor wafer. Then the piece is bonded onto the receptor wafer using the Karl Suss SB6 Bonder (bonding procedure was developed by Anthony Kim and Eilam Morag). Since the ridge lasers are going to have a cleaved facet, extra care must be taken to ensure the piece aligns with the InP receptor wafer orientation. The alignment was done to a great accuracy, as shown in Fig. 4.6a.

Next, the InP substrate was lapped down to around 50 $\mu$m, and the rest was wet etched using HCl:$H_3PO_4$ (1:3) solution. The piece after InP etch is shown in Fig. 4.6a. The etch

rate is around 1 $\mu$m/min, and a magnetic stirring bar was used to ensure etch uniformity. The etch stops at the InGaAs etch stop layer with very high selectivity. Then the InGaAs etch stop layer was etched to minimize loss using a $C_6H_8O_7$:$H_2O_2$ (0.5:1) solution. The etch rate of the InGaAs and AlInAs layers are around 123.5 nm/min and 2.1 nm/min respectively, providing selectivity of  59 [9]. If etched long enough, the underlying AlInAs layer will start to etch, and colorful rings will appear on the surface.

Following the wet etch, a 250 nm of PECVD oxide (1HFSO recipe) was deposited on the surface, which was then patterned using BOE. The reason for using a wet etch instead of dry etch is to have a smooth transition from the oxide layer to the top metal layer.

Next, the top metal (Ti/Au/Ni) is deposited using the CHA e-beam evaporator. The nickle acts as the etch mask for the dry etch of the MQW, and the titanium is the adhesion layer. A few problems were encountered during the lift-off of the metal. First, the small areas between the bridges and the bias pad did not come off as clean, however an application of ultrasonic bath improved the process. And second, the ultrasound caused peeling of the top metal due to the film already having high stress from the nickle. To avoid this problem in the future, a larger area should be used between ridges and the pads in order to avoid using the ultrasonic bath.

The oxide on the pads and bridges was originally made larger to account for any possible mask alignment errors. Therefore, a dry etch step is done to etch any exposed oxide before etching the MQW into ridges. This step should not be skipped as the exposed oxide will mask the MQW etch which will create steps in the etch profile. STS AOE dry etch tool is used with OXIDAPIC recipe for about 70 seconds to etch the oxide. The sample is inspected under microscope to ensure all the exposed oxides are etched away, because any remaining oxide pieces can mask the MQW etch and create nanowires, which although interesting, they are not the intention of our fabrication.

For etching the MQW, the ULVAC NE-550 Chlorine etcher is used. The recipe is developed by the author and the UCLA Nanolab staff, which is a high power chlorine etch at

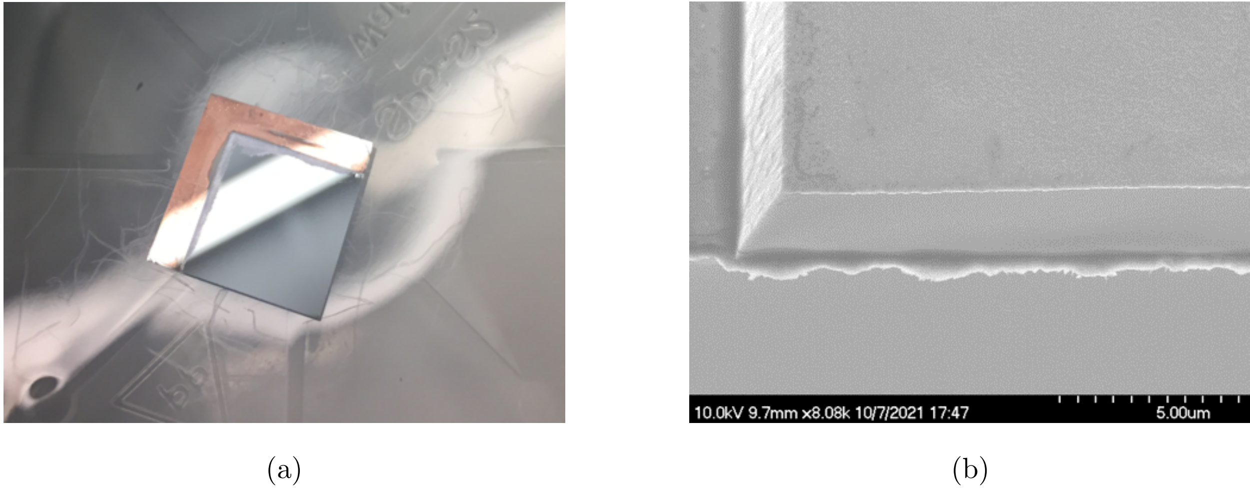


(a) (b)

Figure 4.6: (a) Piece after InP etch using HCl:$H_3PO_4$ (1:3) solution and (b) dry etch profile using ULVAC NE-550 Chlorine etcher.

room temperature using $BCl_3$, Ar, and Cl gases. The $BCl_3$ is used to etch the aluminium in AlInAs, chlorine is the chemical component, and argon acts as the physical agent in the dry etch. The current etch profile, shown in Fig. 4.6b, has a 70 degrees sidewall angle with smooth sidewalls and flat surface at the bottom. It needs to be noted that any exposed thermal grease (applied on the substrate holding the piece) will burn and contaminate the chamber, in addition to affecting the etch profile. In fact, it was seen that the exposed grease can make the surface grassy. This etch recipe is still under development to enhance sidewall angle and make the etch more vertical. Additionally, after the dry etch is complete, the Ni mask is already etched, which eliminates the need to wet-etch the Ni mask.

Finally, a Ti/Au bottom contact is evaporate on the back of the sample to finish the fabrication process.

## 4.5 Device characterization

The fabricated MM waveguide ridges were cleaved into 1 mm laser bars and were characterized using the LIV setup described in Chapter 3. Data were taken using Avtech AVR-

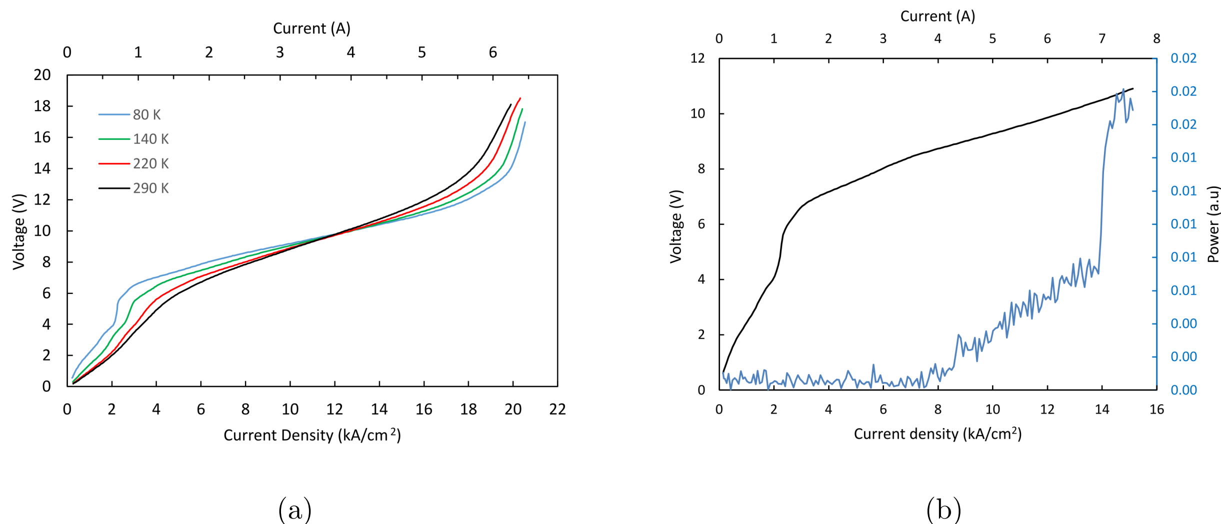


(a)

(b)

Figure 4.7: (a) Current-voltage characteristics of 200 um diameter mesa versus temperature and (b) light-current-voltage characteristics of 50 $\mu$m wide 1 mm length MM waveguide ridge at 78 K.

7B-B-R50 laser diode driver along with 4121B boxcar. To avoid heating and burning of the wirebonds, 250 ns pulses at 5 kHz were used (0.125% duty cycle). The current density-voltage (J-V) characteristics versus temperature of a mesa is shown in Fig. 4.7a. A maximum current density of 20 kA/cm$^2$ was observed, and the subthreshold leakage current decreased when the device was cooled down to 77 K as expected. The LIV of a 50 $\mu$m wide and 1 mm long MM waveguide ridge at 78 K is shown in Fig. 4.7b. A threshold current density of 7 kA/cm$^2$ was observed, which was also apparent in the sudden increase of differential conductance in the IV plot. The device exhibits large dynamic range, which was expected from the lifetime values of lasing levels discussed in section 4.2.

The spectra of the laser was taken using a deuterated triglycine sulfate (DTGS) detector in the FTIR using linear scan. Due to the low power of the laser, and also low transmission of the high-density polyethylene (HDPE) window used on the cryostat and the detector window (around 15-20 %), the alignment was challenging. Therefore, a lock-in amplifier was used to read the detector signal while the mirror scan was stopped, and then the alignment was

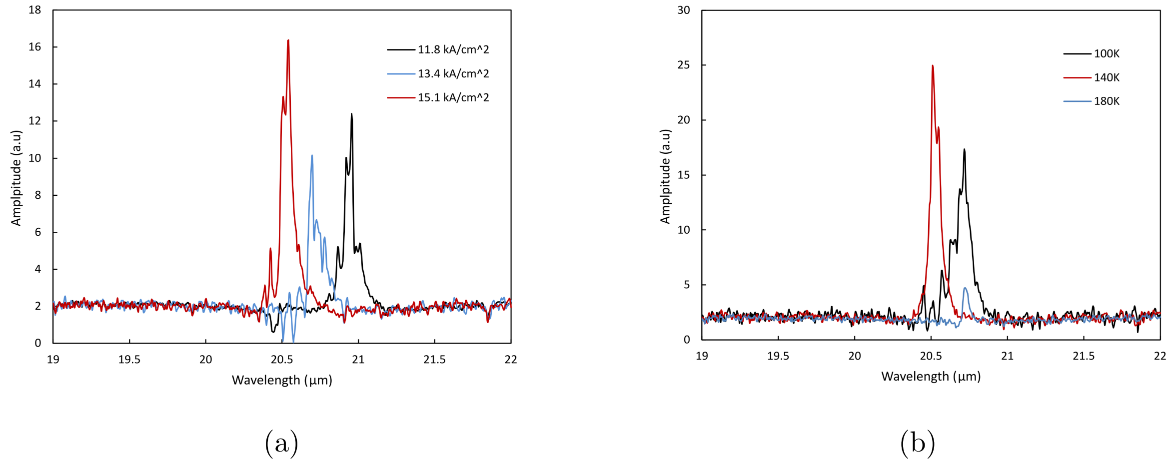


(a) (b)

Figure 4.8: (a) Bias dependent spectra of the 50 $\mu$m wide 1 mm long MM waveguide ridge laser and (b) its temperature dependent spectra.

performed to maximize the signal on the detector. The device lased between 20.4 $\mu$m - 21 $\mu$m with a blue shift occurring with increasing bias as expected, as shown in Fig. 4.8a. The temperature dependent spectra is also shown in Fig. 4.8b, and lasing spectra was detected up to 180 K. However, a maximum operating temperature of the laser is under investigation, and it will likely lase beyond 180 K if power is detected using a sensitive helium-cooled Si bolometer.

This project is still on-going and further results will become available in the coming months.

# CHAPTER 5

# Conclusion

In this thesis, I have developed simulation and transport modelling tools to study and potentially improve the efficiency of quantum cascade lasers for two regions of interest at around 5 $\mu$m and 20 $\mu$m. Additionally, I have developed detailed micro-fabrication process flow for making QC ridge lasers, and have successfully characterized and analyzed multiple devices and active regions. Some of the major accomplishments in this work include:

- Development of a bandstructure simulator that included modeling active regions with two or more compositions using a Schrödinger solver based on the shooting method. The effect of non-parabolicity was included using a three band Kane model, which turned out to be of significant importance. Various scattering mechanisms were implemented, such as longitudinal optical phonon, interface roughness, and alloy disorder scattering, that proved very useful in assessing the designed active regions by calculating lifetimes and gain cross section.

- Development of major fabrication processes for our QCLs, including the wet etch process for the 5 $\mu$m and dry etch for the 20 $\mu$m MM waveguide devices. The overall process flow was also refined to ensure optimum yield for the fabricated devices, and has been used multiple times with high yield.

- Characterization development for testing various properties of our QCLs. This includes measuring temperature dependent pulsed and continuous-wave light-current-voltage characteristics, laser emission power, as well as spectra and electroluminescence mea-

surement. Additionally, capacitance-voltage characterization of THz MM ridge laser was developed, which revealed important average doping values of the active regions, which matches the experimental $J$-$V$ data ($J_{max}$) with great accuracy.

- Design of a QCL that operates around 20 $\mu$m, which is close to the *Reststrahlen* band of III-V semiconductors (20 - 60 $\mu$m). This design was based on a bound-to-continuum design that was used originally to make QCL at 24 $\mu$m [37]. Additionally, electromagnetic simulations of the waveguide was performed using the finite element method solver COMSOL to analyze and manage the losses. Also, micro-fabrication development was done to successfully make a dry etch recipe to make metal-metal ridge waveguides. The device successfully lased and is currently under further development.

The future plans following this work is to continue the characterization of the 20 $\mu$m laser described in Chapter 4, and developing further fabrication for high aspect ratio dry etches.

The QCLs are increasingly becoming the leading choice of coherent sources in mid-infrared regime for many applications in research and industry, and their performance is improving with the most notable being their high wall plug efficiency. Additionally, they are showing great promise for becoming the leading source in the underdeveloped far-infrared region. However, there are still many areas that need further development, from using different semiconductors with new optical and electrical properties such as Al-free III-V, group II-VI, and group IV materials, to improving the growth quality and techniques to ensure defect-free and repeatable structures.

# APPENDIX A

# Fabrication Process Flow

## A.1 Etch mask preparation

| Step | Name | Description | Remarks |
|---|---|---|---|
| 1.1 | Cleave | Gently cleave a 1.5 by 1.5 cm piece using scribe | |
| 1.2 | Solvent Clean | Use Acetone, Methanol, and Isopropanol to clean piece | Removes organic contaminants |
| 1.3 | Oxide Deposition | Deposit around 300 nm of high frequency Silicon oxide using STS – PECVD tool | |
| 1.4 | Dehydration Bake | Bake piece at 150 °C for $\geq$ 5 minutes. Skip this step if piece is just out of PECVD | Drive-off moisture |
| 1.5 | HMDS Coat | Place piece in HMDS beaker for $\geq$ 10 minutes | Improves adhesion |
| 1.6 | Photoresist Coat | Place AZ5214-E photoresist with a dropper and spin at 600/4000 rpm for 6/40 seconds | PR should cover at least two thirds of the piece |
| 1.7 | Prebake Resist | Bake piece on hotplate at 110 °C for one minute | |

| Step | Name | Description | Remarks |
|---|---|---|---|
| 1.8 | Mask Align-ment/ Exposure | Align mask (pattern L1) and expose at 8 W/cm2 for 10 seconds | |
| 1.9 | Development | Develop piece using V(AZ400K):V(H2O)=1:4, 60 seconds, then rinse with water and N2 blow dry | |
| 1.10 | Microscope Inspection | Inspect under microscope and check for under or overdevelopment | |
| 1.11 | Post Bake | Bake piece on hotplate at 120 °C for 2 minutes | Do not post bake without inspection |
| 1.12 | Plasma Descum | Etch piece using Tegal Plasma Etcher at 180 W for one minute | Removes PR residue |
| 1.13 | Wet Etch Oxide | Etch the oxide using Buffered Oxide Etch (BOE) until etch mask pattern is defined | |
| 1.14 | Photoresist Strip | Strip the resist using Matrix Asher and rinse with Acetone | |

## A.2 Ridge definition

| Step | Name | Description | Remarks |
|---|---|---|---|
| 2.1 | Prepare Etchant | Mix HBr:HCl:H2O2:H2O (10:5:1:50) by volume. Add acid to water and add H2O2 last. Wait for 20 minutes for oxidation process to finish | |

| Step | Name | Description | Remarks |
|---|---|---|---|
| 2.2 | Etch piece | Etch piece to one minute. Use Dektak to measure the etch rate, and continue until desired depth is reached | |
| 2.3 | Wet Etch | Etch the oxide mask using BOE | |
| 2.4 | Microscope Inspection | Inspect ridges under microscope | |

## A.3 Top window opening for electrical contact

| Step | Name | Description | Remarks |
|---|---|---|---|
| 3.1 | Oxide Deposition | Deposit around 300 nm of high frequency Silicon oxide using STS – PECVD tool | |
| 3.2 | Dehydration Bake | Bake piece at 150 °C for ≥ 5 minutes. Skip this step if piece is just out of PECVD | Drive-off moisture |
| 3.3 | HMDS Coat | Place piece in HMDS beaker for ≥ 10 minutes | Improves adhesion |
| 3.4 | Photoresist Coat | Place AZ5214-E photoresist with a dropper and spin at 600/4000 rpm for 6/40 seconds | PR should cover at least two thirds of the piece |
| 3.5 | Prebake Resist | Bake piece on hotplate at 110 °C for one minute | |
| 3.6 | Mask Alignment/ Exposure | Align mask (pattern L2) and expose at 8 W/cm2 for 8 seconds | |

| Step | Name | Description | Remarks |
|---|---|---|---|
| 3.7 | Development | Develop piece using V(AZ400K):V(H2O)=1:4, 30 seconds, then rinse with water and N2 blow dry | |
| 3.8 | Microscope Inspection | Inspect under microscope and check for under or overdevelopment | |
| 3.9 | Post Bake | Bake piece on hotplate at 120 °C for 2 minutes | Do not post bake without inspection |
| 3.10 | Plasma Descum | Etch piece using Tegal Plasma Etcher at 180 W for one minute | Removes PR residue |
| 3.11 | Wet Etch Oxide | Etch the oxide using Buffered Oxide Etch (BOE) until the top opening is defined | |
| 3.12 | Photoresist Strip | Strip the resist using Matrix Asher and rinse with Acetone | |

## A.4 Top contact deposition

| Step | Name | Description | Remarks |
|---|---|---|---|
| 4.1 | Dehydration Bake | Bake piece at 150 °C for $\geq$ 5 minutes. | Drive-off moisture |
| 4.2 | HMDS Coat | Place piece in HMDS beaker for $\geq$ 10 minutes | May not be necessary since NLOF is sticky |
| 4.3 | Photoresist Coat | Place NLOF-2020 photoresist with a dropper and spin at 500/2000/4000 rpm for 6/6/30 seconds | PR should cover at least two thirds of the piece |

| Step | Name | Description | Remarks |
|---|---|---|---|
| 4.4 | Prebake Resist | Bake piece on hotplate at 110 °C for one minute | |
| 4.5 | Mask Alignment | Align mask (pattern L3) and expose at 8 W/cm2 for 8 seconds | |
| 4.6 | Post-Exposure Bakev | Bake piece on hotplate at 110 °C for one minute | |
| 4.7 | Development | Develop piece using AZ300MIF 100%, 60 seconds, then rinse with water and N2 blow dry | |
| 4.8 | Microscope Inspection | Inspect under microscope and check for under or overdevelopment | |
| 4.9 | Plasma Descum | Etch piece using Tegal Plasma Etcher at 180 W for one minute | Removes PR residue |
| 4.10 | BOE dip | Dip the piece in Buffered Oxide Etch (BOE) for 2-3 seconds | Removes native oxide |
| 4.11 | Top Contact deposition | Evaporate Ti/Au (20/300 nm) at 15° | Tilted deposition ensures conformal coverage of the ridge sidewall |

## A.5 Substrate lapping and bottom contact deposition

| Step | Name | Description | Remarks |
|---|---|---|---|
| 5.1 | Substrate lapping/ polishing | Lap the substrate using PM5 polisher to around 150 microns. Then polish the substrate for a smooth mirror like finish. | Provides good thermal conduction. |
| 5.2 | BOE dip | Dip the piece in Buffered Oxide Etch (BOE) for 2-3 seconds | Removes native oxide |
| 5.3 | Bottom Contact deposition | Evaporate Ti/Au (20/300 nm) | |

# APPENDIX B

# CV Characterization

Active region doping has always been an essential part of QCL design. While it is necessary for QCL operation and electrical stability, it can limit their performance by introducing ionized impurity scattering which can cause significant gain broadening, and distortions to the conduction band if the doping is very high. This along with the fact that the threshold ($J_{th}$) and maximum current density ($J_{max}$) scale almost linearly with the active region doping makes it a key design parameter. Therefore, accurate knowledge of the doping is helpful in understanding device characteristics, such as difference in $J_{max}$ of two growths of the same QCL design.

Capacitance-Voltage (C-V) characterization is a standard technique used in semiconductor industry to characterize doping in p-n junctions and Schottky diodes. The depletion capacitance of a Schottky diode is give by

$$C = \sqrt{\frac{q\epsilon N_D}{2(V_{bi} - V)}} \tag{B.1}$$

Where $V_{bi}$ is the built-in potential of the Schottky contact and $N_D$ is the average doping density of the semiconductor [45]. From this formula, the average doping concentration can be derived as

$$N_D = \frac{2}{q\epsilon_s}\left[\frac{-1}{d(1/C^2)/dV}\right] \tag{B.2}$$

A QCL with a metal contact directly on the active region (no high doped contact layer) makes a Schottky contact, which can be used to characterize the average QCL doping. The characterization set-up is shown in Figure B.1a. The device under test (DUT), which is

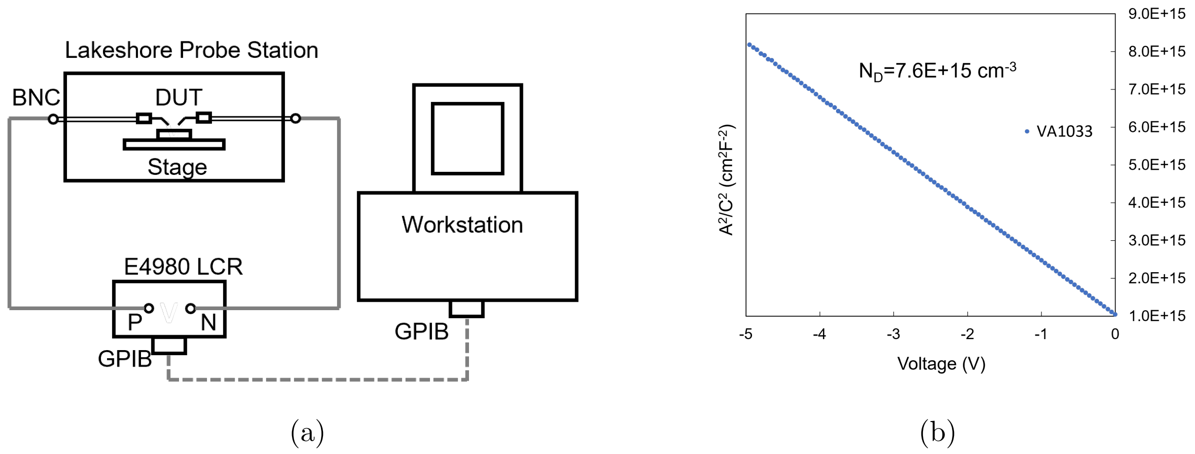


(a) (b)

Figure B.1: (a) Capacitance-voltage characterization setup and (b) C-V measurement of device VA1033

a MM waveguide THz QCL in this case, is probed on top of the waveguide and also on the bottom copper layer (if copper is not exposed, the stage is probed instead). Short and open corrections are performed to account for stray impedance and admittance between the cables and DUT connecting points. Then, a DC sweep is performed with the precision LCR meter, using $C_P - R_P$ mode: 1 MHz frequency, 25 mV bias swing, and the data is collected using LabView software through GPIB cable. The average doping and built-in voltage is then extracted by fitting $1/C^2$ vs. voltage plot, which turned out to be a straight line as is the case for uniformly doped Schottky diodes. An example of a fit is shown for a QCL with average designed doping of $7.1 \times 10^{15} cm^{-3}$ in Figure B.1b.

REFERENCES


[1] Tsuneya Ando, Alan B Fowler, and Frank Stern. Electronic properties of two-dimensional systems. *Reviews of Modern Physics*, 54(2):437, 1982.

[2] Y Bai, N Bandyopadhyay, Slivken Tsao, S Slivken, and Manijeh Razeghi. Room temperature quantum cascade lasers with 27% wall plug efficiency. *Applied Physics Letters*, 98(18):181102, 2011.

[3] G_ Bastard. Superlattice band structure in the envelope-function approximation. *Physical Review B*, 24(10):5693, 1981.

[4] Mattias Beck, Daniel Hofstetter, Thierry Aellen, Jérôme Faist, Ursula Oesterle, Marc Ilegems, Emilio Gini, and Hans Melchior. Continuous wave operation of a mid-infrared semiconductor laser at room temperature. *science*, 295(5553):301–305, 2002.

[5] DJ BenDaniel and CB Duke. Space-charge effects on electron tunneling. *Physical review*, 152(2):683, 1966.

[6] A Bulusu and DG Walker. Modeling of thermoelectric properties of semi-conductor thin films with quantum and scattering effects. 2007.

[7] Zhigao Chen, Jin Wang, Baigeng Wang, and DY Xing. Spin-flip effects on andreev reflection process. *Physics Letters A*, 334(5-6):436–446, 2005.

[8] YenTing Chiu, Yamac Dikmelik, Peter Q Liu, Nyan L Aung, Jacob B Khurgin, and Claire F Gmachl. Importance of interface roughness induced intersubband scattering in mid-infrared quantum cascade lasers. *Applied Physics Letters*, 101(17):171117, 2012.

[9] Gregory C DeSalvo, Wen F Tseng, and James Comas. Etch rates and selectivities of citric acid/hydrogen peroxide on gaas, al0. 3ga0. 7as, in0. 2ga0. 8as, in0. 53ga0. 47as, in0. 52al0. 48as, and inp. *Journal of The Electrochemical Society*, 139(3):831, 1992.

[10] M Carmen Estevez, Mar Alvarez, and Laura M Lechuga. Integrated optical devices for lab-on-a-chip biosensing applications. *Laser & Photonics Reviews*, 6(4):463–487, 2012.

[11] Jérôme Faist. Wallplug efficiency of quantum cascade lasers: Critical parameters and fundamental limits. *Applied physics letters*, 90(25):253512, 2007.

[12] Jérôme Faist. *Quantum cascade lasers*. OUP Oxford, 2013.

[13] Jérôme Faist, Mattias Beck, Thierry Aellen, and Emilio Gini. Quantum-cascade lasers based on a bound-to-continuum transition. *Applied Physics Letters*, 78(2):147–149, 2001.

[14] Jerome Faist, Federico Capasso, Deborah L Sivco, Carlo Sirtori, Albert L Hutchinson, and Alfred Y Cho. Quantum cascade laser. *Science*, 264(5158):553–556, 1994.

[15] K Feng, W Streyer, Y Zhong, AJ Hoffman, and D Wasserman. Photonic materials, structures and devices for reststrahlen optics. *Optics express*, 23(24):A1418–A1433, 2015.

[16] Lucia Fernández-Carrasco, D Torrens-Martín, LM Morales, and Sagrario Martínez-Ramírez. Infrared spectroscopy in the analysis of building and construction materials. *Infrared spectroscopy–Materials science, engineering and technology*, pages 369–382, 2012.

[17] Martin Franckié, Lorenzo Bosco, Mattias Beck, Christopher Bonzon, Elena Mavrona, Giacomo Scalari, Andreas Wacker, and Jérôme Faist. Two-well quantum cascade laser optimization by non-equilibrium green's function modelling. *Applied Physics Letters*, 112(2):021104, 2018.

[18] Thomas Grange, David Stark, Giacomo Scalari, Jérôme Faist, Luca Persichetti, Luciana Di Gaspare, Monica De Seta, Michele Ortolani, Douglas J Paul, Giovanni Capellini, et al. Room temperature operation of n-type ge/sige terahertz quantum cascade lasers predicted by non-equilibrium green's functions. *Applied Physics Letters*, 114(11):111102, 2019.

[19] PK Gupta and SC Mehendale. Mid-infrared optically pumped molecular lasers. *Hyperfine Interactions*, 37(1):243–273, 1987.

[20] Paul Harrison and Alex Valavanis. *Quantum wells, wires and dots: theoretical and computational physics of semiconductor nanostructures*. John Wiley & Sons, 2016.

[21] Seokmin Hong, Vinh Diep, Supriyo Datta, and Yong P Chen. Modeling potentiometric measurements in topological insulators including parallel channels. *Physical Review B*, 86(8):085131, 2012.

[22] Siyuan Hou, Christopher B Riley, Cynthia A Mitchell, R Anthony Shaw, Janet Bryanton, Kathryn Bigsby, and J Trenton McClure. Exploration of attenuated total reflectance mid-infrared spectroscopy and multivariate calibration to measure immunoglobulin g in human sera. *Talanta*, 142:110–119, 2015.

[23] Christian Jirauschek and Tillmann Kubis. Modeling techniques for quantum cascade lasers. *Applied Physics Reviews*, 1(1):011307, 2014.

[24] Pierre Jouy, Markus Mangold, Béla Tuzson, Lukas Emmenegger, Yu-Chi Chang, Lubos Hvozdara, Hans Peter Herzig, Philip Wägli, Alexandra Homsy, Nico F de Rooij, et al. Mid-infrared spectroscopy for gases and liquids based on quantum cascade technologies. *Analyst*, 139(9):2039–2046, 2014.

[25] D Jung, S Bank, Minjoo Lawrence Lee, and D Wasserman. Next-generation mid-infrared sources. *Journal of Optics*, 19(12):123001, 2017.

[26] Leo P Kadanoff and Gordon Baym. *Quantum statistical mechanics*. 1962.

[27] Evan O Kane. Band structure of indium antimonide. *Journal of Physics and Chemistry of Solids*, 1(4):249–261, 1957.

[28] Mustafa Kansiz, Helen Billman-Jacobe, and Don McNaughton. Quantitative determination of the biodegradable polymer poly ($\beta$-hydroxybutyrate) in a recombinant escherichia coli strain by use of mid-infrared spectroscopy and multivariative statistics. *Applied and environmental microbiology*, 66(8):3415–3420, 2000.

[29] R Kazarinov. Possibility of amplification of electromagnetic waves in a semiconductor with superlattice. *Sov. Phys.-Semicond.*, 5(4):707–709, 1971.

[30] Leonid V Keldysh et al. Diagram technique for nonequilibrium processes. *Sov. Phys. JETP*, 20(4):1018–1026, 1965.

[31] Jacob B Khurgin, Yamac Dikmelik, Peter Q Liu, Anthony J Hoffman, Matthew D Escarra, Kale J Franz, and Claire F Gmachl. Role of interface roughness in the transport and lasing characteristics of quantum-cascade lasers. *Applied Physics Letters*, 94(9):091101, 2009.

[32] Herbert Kroemer. Heterostructure bipolar transistors and integrated circuits. *Proceedings of the IEEE*, 70(1):13–25, 1982.

[33] Hongtao Lin, Lan Li, Yi Zou, Okechukwu Ogbuu, Sylvain Danto, J David Musgraves, Kathleen Richardson, and Juejun Hu. Chalcogenide glass planar photonics: from mid-ir sensing to 3-d flexible substrate integration. In *Laser Resonators, Microresonators, and Beam Control XV*, volume 8600, page 86000K. International Society for Optics and Photonics, 2013.

[34] A Lyakh, M Suttinger, R Go, P Figueiredo, and A Todi. 5.6 $\mu$ m quantum cascade lasers based on a two-material active region composition with a room temperature wall-plug efficiency exceeding 28%. *Applied Physics Letters*, 109(12):121109, 2016.

[35] R Martini and EA Whittaker. Quantum cascade laser-based free space optical communications. In *Free-Space Laser Communications*, pages 393–406. Springer, 2005.

[36] Michal Nikodem and Gerard Wysocki. Chirped laser dispersion spectroscopy for remote open-path trace-gas sensing. *Sensors*, 12(12):16466–16481, 2012.

[37] K Ohtani, M Beck, and Jérôme Faist. Double metal waveguide ingaas/alinas quantum cascade lasers emitting at 24 $\mu$ m. *Applied Physics Letters*, 105(12):121115, 2014.

[38] G Pegolloti. *Quantum engineering of collective states in semiconductor nanostructures.* PhD thesis, 2011.

[39] Manijeh Razeghi. High-performance inp-based mid-ir quantum cascade lasers. *IEEE Journal of Selected Topics in Quantum Electronics*, 15(3):941–951, 2009.

[40] Benedikt Schwarz, Peter Reininger, Daniela Ristanić, Hermann Detz, Aaron Maxwell Andrews, Werner Schrenk, and Gottfried Strasser. Monolithically integrated mid-infrared lab-on-a-chip using plasmonics and quantum cascade structures. *Nature communications*, 5(1):1–7, 2014.

[41] Carlo Sirtori, Federico Capasso, Jérôme Faist, and Sandro Scandolo. Nonparabolicity and a sum rule associated with bound-to-bound and bound-to-continuum intersubband transitions in quantum wells. *Physical Review B*, 50(12):8663, 1994.

[42] S B Slivken. *Quantum cascade lasers grown by gas-source molecular beam epitaxy.* PhD thesis, 2002.

[43] J H Smet. *Intrawell and Interwell Intersubband Transitions in Single and Multiple Quantum Well Heterostructures.* PhD thesis, 1995.

[44] In Keun Son and Shiwen Mao. A survey of free space optical networks. *Digital communications and networks*, 3(2):67–77, 2017.

[45] Simon M Sze and Kwok K Ng. *Physics of semiconductor devices.* John wiley & sons, 2007.

[46] R L Terazzi. *Transport in quantum cascade lasers.* PhD thesis, 2012.

[47] Karl Unterrainer, Raffaele Colombelli, Claire Gmachl, Federico Capasso, Harold Y Hwang, A Michael Sergent, Deborah L Sivco, and Alfred Y Cho. Quantum cascade lasers with double metal-semiconductor waveguide resonators. *Applied physics letters*, 80(17):3060–3062, 2002.

[48] Takeya Unuma, Teruyuki Takahashi, Takeshi Noda, Masahiro Yoshita, Hiroyuki Sakaki, Motoyoshi Baba, and Hidefumi Akiyama. Effects of interface roughness and phonon scattering on intersubband absorption linewidth in a gaas quantum well. *Applied Physics Letters*, 78(22):3448–3450, 2001.

[49] Takeya Unuma, Masahiro Yoshita, Takeshi Noda, Hiroyuki Sakaki, and Hidefumi Akiyama. Intersubband absorption linewidth in gaas quantum wells due to scattering by interface roughness, phonons, alloy disorder, and impurities. *Journal of applied physics*, 93(3):1586–1597, 2003.

[50] Angela Vasanelli, A Leuliet, C Sirtori, A Wade, G Fedorov, D Smirnov, G Bastard, B Vinter, M Giovannini, and Jérôme Faist. Role of elastic scattering mechanisms in ga in as/ al in as quantum cascade lasers. *Applied physics letters*, 89(17):172120, 2006.

[51] Andreas Wacker. Semiconductor superlattices: a model system for nonlinear transport. *Physics Reports*, 357(1):1–111, 2002.

[52] Andreas Wacker, Martin Lindskog, and David O Winge. Nonequilibrium green's function model for simulation of quantum cascade laser devices under operating conditions. *IEEE Journal of Selected Topics in Quantum Electronics*, 19(5):1–11, 2013.

[53] F Wang, S Slivken, DH Wu, and M Razeghi. Room temperature quantum cascade laser with 31% wall-plug efficiency. *AIP Advances*, 10(7):075012, 2020.

[54] F Wang, S Slivken, DH Wu, and M Razeghi. Room temperature quantum cascade lasers with 22% wall plug efficiency in continuous-wave operation. *Optics Express*, 28(12):17532–17538, 2020.

[55] B S Williams. *Terahertz quantum cascade lasers*. PhD thesis, 2003.

[56] Andreas Wittmann, Yargo Bonetti, Jérôme Faist, Emilio Gini, and Marcella Giovannini. Intersubband linewidths in quantum cascade laser designs. *Applied Physics Letters*, 93(14):141103, 2008.

[57] Q Yang, R Lösch, W Bronner, S Hugger, F Fuchs, R Aidam, and J Wagner. onhigh-peak-power strain-compensated gainas/alinas quantum cascade lasers ($\lambda$ 4.6 $\mu$ m) based on a slightly diagonal active region design. *Applied Physics Letters*, 93(25):251110, 2008.

[58] Yariv. *Quantum Electronics*. John Wiley & Sons, 1989.

[59] Wenjia Zhou, Quan-Yong Lu, Dong-Hai Wu, Steven Slivken, and Manijeh Razeghi. High-power, continuous-wave, phase-locked quantum cascade laser arrays emitting at 8 $\mu$m. *Optics express*, 27(11):15776–15785, 2019.